

Search for charged Higgs bosons in e^+e^- collisions at $\sqrt{s} = 189\text{--}209\text{ GeV}$

The OPAL Collaboration

G. Abbiendi², C. Ainsley⁵, P.F. Åkesson⁷, G. Alexander²¹, G. Anagnostou¹, K.J. Anderson⁸, S. Asai^{22,23}, D. Axen²⁷, I. Bailey²⁶, E. Barberio^{7,r}, T. Barillari³², R.J. Barlow¹⁵, R.J. Batley⁵, P. Bechtle²⁵, T. Behnke²⁵, K.W. Bell¹⁹, P.J. Bell¹, G. Bella²¹, A. Bellerive⁶, G. Benelli⁴, S. Bethke³², O. Biebel³¹, O. Boeriu⁹, P. Bock¹⁰, M. Boutemour³¹, S. Braibant², R.M. Brown¹⁹, H.J. Burckhart⁷, S. Campana⁴, P. Capiluppi², R.K. Carnegie⁶, A.A. Carter¹², J.R. Carter⁵, C.Y. Chang¹⁶, D.G. Charlton¹, C. Ciocca², A. Csilling²⁹, M. Cuffiani², S. Dado²⁰, M. Dallavalle², A. De Roeck⁷, E.A. De Wolf^{7,u}, K. Desch²⁵, B. Dienes³⁰, J. Dubbert³¹, E. Duchovni²⁴, G. Duckeck³¹, I.P. Duerdoth¹⁵, E. Etzion²¹, F. Fabbri², P. Ferrari⁷, F. Fiedler³¹, I. Fleck⁹, M. Ford¹⁵, A. Frey⁷, P. Gagnon¹¹, J.W. Gary⁴, C. Geich-Gimbel³, G. Giacomelli², P. Giacomelli², M. Giunta⁴, J. Goldberg²⁰, E. Gross²⁴, J. Grunhaus²¹, M. Gruwé⁷, A. Gupta⁸, C. Hajdu²⁹, M. Hamann²⁵, G.G. Hanson⁴, A. Harel²⁰, M. Hauschild⁷, C.M. Hawkes¹, R. Hawkings⁷, G. Herten⁹, R.D. Heuer²⁵, J.C. Hill⁵, K. Hoffman¹⁶, D. Horváth^{29,e}, P. Igo-Kemenes¹⁰, K. Ishii^{22,23}, H. Jeremie¹⁷, P. Jovanovic¹, T.R. Junk^{6,k}, J. Kanzaki^{22,23,w}, D. Karlen²⁶, K. Kawagoe^{22,23}, T. Kawamoto^{22,23}, R.K. Keeler²⁶, R.G. Kellogg¹⁶, B.W. Kennedy¹⁹, S. Kluth³², T. Kobayashi^{22,23}, M. Kobel^{3,v}, S. Komamiya^{22,23}, T. Krämer²⁵, A. Krasznahorkay Jr.^{30,g}, P. Krieger^{6,n}, J. von Krogh¹⁰, T. Kuhl²⁵, M. Kupper²⁴, G.D. Lafferty¹⁵, H. Landsman²⁰, D. Lanske¹³, D. Lellouch²⁴, J. Letts^q, L. Levinson²⁴, J. Lillich⁹, S.L. Lloyd¹², F.K. Loebinger¹⁵, J. Lu^{27,d}, A. Ludwig^{3,v}, J. Ludwig⁹, W. Mader^{3,v}, S. Marcellini², T.E. Marchant¹⁵, A.J. Martin¹², T. Mashimo^{22,23}, P. Mättig^o, J. McKenna²⁷, R.A. McPherson²⁶, F. Meijers⁷, W. Menges²⁵, F.S. Merritt⁸, H. Mes^{6,c}, N. Meyer²⁵, A. Michelini², S. Mihara^{22,23}, G. Mikenberg²⁴, D.J. Miller¹⁴, W. Mohr⁹, T. Mori^{22,23}, A. Mutter⁹, K. Nagai¹², I. Nakamura^{22,23,x}, H. Nanjo^{22,23}, H.A. Neal³³, S.W. O’Neale^{1,b}, A. Oh⁷, A. Okpara¹⁰, M.J. Oreglia⁸, S. Orito^{22,23,b}, C. Pahl³², G. Pásztor^{4,i}, J.R. Pater¹⁵, J.E. Pilcher⁸, J. Pinfold²⁸, D.E. Plane⁷, O. Pooth¹³, M. Przybycień^{7,p}, A. Quadt³², K. Rabbertz^{7,t}, C. Rembser⁷, P. Renkel²⁴, J.M. Roney²⁶, A.M. Rossi², Y. Rozen²⁰, K. Runge⁹, K. Sachs⁶, T. Saeki^{22,23}, E.K.G. Sarkisyan^{7,l}, A.D. Schaile³¹, O. Schaile³¹, P. Scharff-Hansen⁷, J. Schieck³², T. Schörner-Sadenius^{7,ab}, M. Schröder⁷, M. Schumacher³, R. Seuster^{13,h}, T.G. Shears^{7,j}, B.C. Shen^{4,b}, P. Sherwood¹⁴, A. Skuja¹⁶, A.M. Smith⁷, R. Sobie²⁶, S. Söldner-Rembold¹⁵, F. Spano^{8,z}, A. Stahl¹³, D. Strom¹⁸, R. Ströhmer³¹, S. Tarem²⁰, M. Tasevsky^{7,f}, R. Teuscher⁸, M.A. Thomson⁵, E. Torrence¹⁸, D. Toya^{22,23}, I. Trigger^{7,y}, Z. Trócsányi^{30,g}, E. Tsur²¹, M.F. Turner-Watson¹, I. Ueda^{22,23}, B. Ujvári^{30,g}, C.F. Vollmer³¹, P. Vannerem⁹, R. Vértesi^{30,g}, M. Verzocchi¹⁶, H. Voss^{7,s}, J. Vossebeld^{7,j}, C.P. Ward⁵, D.R. Ward⁵, P.M. Watkins¹, A.T. Watson¹, N.K. Watson¹, P.S. Wells^{7,a}, T. Wengler⁷, N. Vermes³, G.W. Wilson^{15,m}, J.A. Wilson¹, G. Wolf²⁴, T.R. Wyatt¹⁵, S. Yamashita^{22,23}, D. Zer-Zion⁴, L. Zivkovic²⁰

¹School of Physics and Astronomy, University of Birmingham, Birmingham B15 2TT, UK

²Dipartimento di Fisica dell’ Università di Bologna and INFN, 40126 Bologna, Italy

³Physikalisches Institut, Universität Bonn, 53115 Bonn, Germany

⁴Department of Physics and Astronomy, University of California, Riverside, CA 92521, USA

⁵Cavendish Laboratory, Cambridge CB3 0HE, UK

⁶Ottawa-Carleton Institute for Physics, Department of Physics, Carleton University, Ottawa, Ontario K1S 5B6, Canada

⁷CERN, European Organisation for Nuclear Research, 1211 Geneva 23, Switzerland

⁸Enrico Fermi Institute and Department of Physics, University of Chicago, Chicago IL 60637, USA

⁹Fakultät für Physik, Albert-Ludwigs-Universität Freiburg, 79104 Freiburg, Germany

¹⁰Physikalisches Institut, Universität Heidelberg, 69120 Heidelberg, Germany

¹¹Department of Physics, Indiana University, Bloomington, IN 47405, USA

¹²Queen Mary and Westfield College, University of London, London E1 4NS, UK

¹³III Physikalisches Institut, Technische Hochschule Aachen, Sommerfeldstrasse 26-28, 52056 Aachen, Germany

¹⁴University College London, London WC1E 6BT, UK

¹⁵School of Physics and Astronomy, Schuster Laboratory, The University of Manchester, Manchester M13 9PL, UK

¹⁶Department of Physics, University of Maryland, College Park, MD 20742, USA

¹⁷Laboratoire de Physique Nucléaire, Université de Montréal, Montréal, Québec H3C 3J7, Canada

¹⁸Department of Physics, University of Oregon, Eugene, OR 97403, USA

- ¹⁹Rutherford Appleton Laboratory, Chilton, Didcot, Oxfordshire OX11 0QX, UK
²⁰Department of Physics, Technion-Israel Institute of Technology, Haifa 32000, Israel
²¹Department of Physics and Astronomy, Tel Aviv University, Tel Aviv 69978, Israel
²²International Centre for Elementary Particle Physics and Department of Physics, University of Tokyo, Tokyo 113-0033, Japan
²³Kobe University, Kobe 657-8501, Japan
²⁴Particle Physics Department, Weizmann Institute of Science, Rehovot 76100, Israel
²⁵Institut für Experimentalphysik, Universität Hamburg/DESY, Notkestrasse 85, 22607 Hamburg, Germany
²⁶Department of Physics, University of Victoria, PO Box 3055, Victoria BC V8W 3P6, Canada
²⁷Department of Physics, University of British Columbia, Vancouver BC V6T 1Z1, Canada
²⁸Department of Physics, University of Alberta, Edmonton AB T6G 2J1, Canada
²⁹Research Institute for Particle and Nuclear Physics, 1525 Budapest, PO Box 49, Hungary
³⁰Institute of Nuclear Research, 4001 Debrecen, PO Box 51, Hungary
³¹Sektion Physik, Ludwig-Maximilians-Universität München, Am Coulombwall 1, 85748 Garching, Germany
³²Max-Planck-Institute für Physik, Föhringer Ring 6, 80805 München, Germany
³³Department of Physics, Yale University, New Haven, CT 06520, USA

Received: 14 October 2008 / Revised: 22 June 2012 / Published online: 24 July 2012
 © The Author(s) 2012. This article is published with open access at Springerlink.com

Abstract A search is made for charged Higgs bosons predicted by Two-Higgs-Doublet extensions of the Standard Model (2HDM) using electron-positron collision data collected by the OPAL experiment at $\sqrt{s} = 189\text{--}209$ GeV, corresponding to an integrated luminosity of approximately 600 pb^{-1} . Charged Higgs bosons are assumed to be pair-produced and to decay into $q\bar{q}$, $\tau\nu_\tau$ or $AW^{\pm*}$. No signal is observed. Model-independent limits on the charged Higgs-boson production cross section are derived by combining these results with previous searches at lower energies. Under the assumption $\text{BR}(H^\pm \rightarrow \tau\nu_\tau) + \text{BR}(H^\pm \rightarrow q\bar{q}) = 1$, motivated by general 2HDM type II models, excluded areas on the $[m_{H^\pm}, \text{BR}(H^\pm \rightarrow \tau\nu_\tau)]$ plane are presented and charged Higgs bosons are excluded up to a mass of 76.3 GeV at

95 % confidence level, independent of the branching ratio $\text{BR}(H^\pm \rightarrow \tau\nu_\tau)$. A scan of the 2HDM type I model parameter space is performed and limits on the Higgs-boson masses m_{H^\pm} and m_A are presented for different choices of $\tan\beta$.

1 Introduction

In the Standard Model (SM) [1–3], the electroweak symmetry is broken via the Higgs mechanism [4–6] generating the masses of elementary particles. This requires the introduction of a complex scalar Higgs-field doublet and implies the existence of a single neutral scalar particle, the Higgs boson. While the SM accurately describes the interactions between elementary particles, it leaves several fundamental questions unanswered. Therefore, it is of great interest to study extended models.

^a e-mail: Pippa.Wells@cern.ch

^b Deceased.

^c Also at TRIUMF, Vancouver, Canada V6T 2A3.

^d Now at University of Alberta.

^e Also at Institute of Nuclear Research, Debrecen, Hungary.

^f Now at Institute of Physics, Academy of Sciences of the Czech Republic 18221 Prague, Czech Republic.

^g Also at Department of Experimental Physics, University of Debrecen, Hungary.

^h Also at MPI München.

ⁱ Also at Research Institute for Particle and Nuclear Physics, Budapest, Hungary.

^j Now at University of Liverpool, Dept of Physics, Liverpool L69 3BX, UK.

^k Now at Dept. Physics, University of Illinois at Urbana-Champaign, USA.

^l Now at University of Texas at Arlington, Department of Physics, Arlington, TX 76019, USA.

^m Now at University of Kansas, Dept of Physics and Astronomy, Lawrence, KS 66045, USA.

ⁿ Now at University of Toronto, Dept of Physics, Toronto, Canada.

^o Now at Bergische Universität, Wuppertal, Germany.

^p Now at University of Mining and Metallurgy, Cracow, Poland.

^q Now at University of California, San Diego, USA.

^r Now at The University of Melbourne, Victoria, Australia.

^s Now at IPHE Université de Lausanne, 1015 Lausanne, Switzerland.

^t Now at IEKP Universität Karlsruhe, Germany.

^u Now at University of Antwerpen, Physics Department, B-2610 Antwerpen, Belgium; supported by Interuniversity Attraction Poles Programme, Belgian Science Policy.

^v Now at Technische Universität, Dresden, Germany.

^w Also at High Energy Accelerator Research Organisation (KEK), Tsukuba, Ibaraki, Japan.

^x Now at University of Pennsylvania, Philadelphia, Pennsylvania, USA.

^y Now at TRIUMF, Vancouver, Canada.

^z Now at Columbia University.

^{aa} Now at CERN.

^{ab} Now at DESY.

The minimal extension of the SM Higgs sector required, for example, by supersymmetric models contains two Higgs-field doublets [7] resulting in five Higgs bosons: two charged (H^\pm) and three neutral. If CP-conservation is assumed, the three neutral Higgs bosons are CP-eigenstates: h and H are CP-even and A is CP-odd. Two-Higgs-Doublet Models (2HDMs) are classified according to the Higgs-fermion coupling structure. In type I models (2HDM(I)) [8, 9], all quarks and leptons couple to the same Higgs doublet, while in type II models (2HDM(II)) [10], down-type fermions couple to the first Higgs doublet, and up-type fermions to the second.

Charged Higgs bosons are expected to be pair-produced in the process $e^+e^- \rightarrow H^+H^-$ at LEP, the reaction $e^+e^- \rightarrow H^\pm W^\mp$ having a much lower cross section [11]. In 2HDMs, the tree-level cross section [12] for pair production is completely determined by the charged Higgs-boson mass and known SM parameters.

The H^\pm branching ratios are model-dependent. In most of the 2HDM(II) parameter space, charged Higgs bosons decay into the heaviest kinematically allowed fermions, namely $\tau\nu_\tau$ and quark pairs.¹ The situation changes in 2HDM(I), where the decay $H^\pm \rightarrow AW^{\pm*}$ can become dominant if the ratio of the vacuum expectation values of the two Higgs-field doublets is such that $\tan\beta \gtrsim 1$ and the A boson is sufficiently light [13, 14].

In this paper we search for charged Higgs bosons decaying into $q\bar{q}$, $\tau\nu_\tau$ and $AW^{\pm*}$ using the data collected by the OPAL Collaboration in 1998–2000. The results are interpreted within general 2HDM(II) assuming $\text{BR}(H^\pm \rightarrow \tau\nu_\tau) + \text{BR}(H^\pm \rightarrow q\bar{q}) = 1$ for the branching ratios and in 2HDM(I) taking into account decays of charged Higgs bosons via $AW^{\pm*}$, as well. Our result is not confined to $q\bar{q} = \{c\bar{s}, \bar{c}s\}$ although that is the dominant hadronic decay channel in most of the parameter space.

The previously published OPAL lower limit on the charged Higgs-boson mass, under the assumption of $\text{BR}(H^\pm \rightarrow \tau\nu_\tau) + \text{BR}(H^\pm \rightarrow q\bar{q}) = 1$, is $m_{H^\pm} > 59.5$ GeV at 95 % confidence level (CL) using data collected at $\sqrt{s} \leq 183$ GeV [15, 16]. Lower bounds of 74.4–79.3 GeV have been reported by the other LEP collaborations [17–19] based on the full LEP2 data set. The DELPHI Collaboration also performed a search for $H^\pm \rightarrow AW^{\pm*}$ decay and constrained the charged Higgs-boson mass in 2HDM(I) [18] to be $m_{H^\pm} \geq 76.7$ GeV at 95 %CL.

¹Throughout this paper charge conjugation is implied. For simplicity, the notation $\tau\nu_\tau$ stands for $\tau^+\nu_\tau$ and $\tau^-\bar{\nu}_\tau$ and $q\bar{q}$ for a quark and anti-quark of any flavor combination.

2 Experimental considerations

The OPAL detector is described in [20–23]. The events are reconstructed from charged-particle tracks and energy deposits (*clusters*) in the electromagnetic and hadron calorimeters. The tracks and clusters must pass a set of quality requirements similar to those used in previous OPAL Higgs-boson searches [24]. In calculating the total visible energies and momenta of events and individual jets, corrections are applied to prevent double-counting of energy in the case of tracks and associated clusters [24].

The data analyzed in this paper were collected in 1998–2000 at center-of-mass energies of 189–209 GeV as given in Table 1. Due to different requirements on the operational state of the OPAL subdetectors, the integrated luminosity of about 600 pb^{-1} differs slightly among search channels.

In this paper the following final states are sought:

- $H^+H^- \rightarrow \tau^+\nu_\tau\tau^-\bar{\nu}_\tau$ (*two-tau final state*, 2τ),
- $H^+H^- \rightarrow q\bar{q}\tau\nu_\tau$ (*two-jet plus tau final state*, $2j + \tau$),
- $H^+H^- \rightarrow q\bar{q}q\bar{q}$ (*four-jet final state*, $4j$),
- $H^+H^- \rightarrow AW^{+*}AW^{-*} \rightarrow b\bar{b}q\bar{q}b\bar{b}q\bar{q}$ (*eight-jet final state*, $8j$),
- $H^+H^- \rightarrow AW^{+*}AW^{-*} \rightarrow b\bar{b}q\bar{q}b\bar{b}\ell\nu_\ell$ (*six-jet plus lepton final state*, $6j + \ell$),
- $H^+H^- \rightarrow AW^{\pm*}\tau\nu_\tau \rightarrow b\bar{b}q\bar{q}\tau\nu_\tau$ (*four-jet plus tau final state*, $4j + \tau$).

The signal detection efficiencies and accepted background cross sections are estimated using a variety of Monte Carlo samples. The HZHA generator [25] is used to simulate H^+H^- production at fixed values of the charged Higgs-boson mass in steps of 1–5 GeV from the kinematic limit down to 50 GeV for fermionic decays and 40 GeV for bosonic decays.

The background processes are simulated primarily by the following event generators: PYTHIA [26, 27] and KK2F [28, 29] ($Z/\gamma^* \rightarrow q\bar{q}(\gamma)$), grc4f [30, 31] (four-fermion processes, $4f$), BHWIDE [32] and TEEGG [33] ($e^+e^-(\gamma)$), KORALZ [34] and KK2F ($\mu^+\mu^-(\gamma)$ and $\tau^+\tau^-(\gamma)$), PHOJET [35, 36], HERWIG [37], Vermaseren [38] (hadronic and leptonic two-photon processes).

The generated partons, both for the signal and the SM Monte Carlo simulations, are hadronized using JETSET [26, 27], with parameters described in [39]. For systematic studies, cluster fragmentation implemented in HERWIG for the process $Z/\gamma^* \rightarrow q\bar{q}(\gamma)$ is used. The predictions of $4f$ processes are cross-checked using EXCALIBUR [40], KoraiW [41] and KandY [42].

The obtained Monte Carlo samples are processed through a full simulation of the OPAL detector [43]. The event selection is described below.

Table 1 Data-taking year, center-of-mass energy bins, luminosity-weighted average center-of-mass energies, the energies of signal and background Monte Carlo simulations, and integrated luminosities of

| Year | 1998 | 1999 | | | | 2000 |
|--|---------|---------|---------|---------|---------|---------|
| E_{cm} (GeV) | 186–190 | 190–194 | 194–198 | 198–201 | 201–203 | 200–209 |
| $\langle E_{\text{cm}} \rangle$ (GeV) | 188.6 | 191.6 | 195.5 | 199.5 | 201.9 | 206.0 |
| $E_{\text{cm}}^{\text{MC}}$ (GeV) | 189 | 192 | 196 | 200 | 202 | 206 |
| $\int \mathcal{L} dt$ (pb $^{-1}$) (2 τ) | 183.5 | 29.3 | 76.4 | 76.6 | 45.5 | 212.6 |
| $\int \mathcal{L} dt$ (pb $^{-1}$) (2j + τ , 4j) | 179.6 | 29.3 | 76.3 | 75.9 | 36.6 | 217.4 |
| $\int \mathcal{L} dt$ (pb $^{-1}$) (8j, 6j + ℓ , 4j + τ) | 175.0 | 28.9 | 74.8 | 77.2 | 36.1 | 211.1 |

the data. The data correspond to total integrated luminosities of 623.9 pb $^{-1}$ for the two-tau, 615.1 pb $^{-1}$ for the two-jet plus tau and the four-jet channels and 603.1 pb $^{-1}$ for the $H^{\pm} \rightarrow AW^{\pm*}$ selections

3 Search for four-fermion final states

In most of the parameter space of 2HDM(II) and with a sufficiently heavy A boson in 2HDM(I), the fermionic decays of the charged Higgs boson dominate and lead to four-fermion final states. The most important decay mode is typically $H^{\pm} \rightarrow \tau \nu_{\tau}$, with the hadronic mode $H^{\pm} \rightarrow q\bar{q}$ reaching about 40 % branching ratio at maximum.

The search for the fully leptonic final state $H^+H^- \rightarrow \tau^+ \nu_{\tau} \tau^- \bar{\nu}_{\tau}$ is described in [44]. The searches for the $H^+H^- \rightarrow q\bar{q}\tau \nu_{\tau}$ and the $H^+H^- \rightarrow q\bar{q}q\bar{q}$ events are optimized using Monte Carlo simulation of $H^+ \rightarrow c\bar{s}$ decays. The sensitivities to other quark flavors are similar and the possible differences are taken into account as systematic uncertainties. Therefore, our results are valid for any hadronic decay of the charged Higgs boson.

Four-fermion final states originating from H^+H^- production would have very similar kinematic properties to W^+W^- production, which therefore constitutes an irreducible background to our searches, especially when $m_{H^{\pm}}$ is close to $m_{W^{\pm}}$. To suppress this difficult SM background, a mass-dependent likelihood selection (similar to the technique described in [45]) is introduced. For each charged Higgs-boson mass tested (m_{test}), a specific analysis optimized for a reference mass (m_{ref}) close to the hypothesized value is used.

We have chosen a set of reference charged Higgs-boson masses at which signal samples are generated. Around these reference points, mass regions (labeled by m_{ref}) are defined with the borders centered between the neighboring points. For each individual mass region, at each center-of-mass energy, we create a separate likelihood selection. The definition of the likelihood function is based on a set of histograms of channel specific observables, given in [16]. The signal histograms are built using events generated at m_{ref} . The background histograms are composed of the SM processes and are identical for all mass regions.

When testing the hypothesis of a signal with mass m_{test} , the background and data rate and discriminant (i.e. the reconstructed Higgs-boson mass) distribution depend on the

mass region to which m_{test} belongs. The signal quantities depend on the value of m_{test} itself and are determined as follows. The signal rate and discriminant distribution are computed, with the likelihood selection optimized for m_{ref} , for three simulated signal samples with masses m_{low} , m_{ref} and m_{high} . Here, m_{low} and m_{high} are the closest mass points to m_{ref} at which signal Monte Carlo samples are generated, with $m_{\text{low}} < m_{\text{ref}} < m_{\text{high}}$. The signal rate and discriminant distribution for m_{test} are then calculated by linear interpolation from the quantities for m_{low} and m_{ref} if $m_{\text{test}} < m_{\text{ref}}$, or for m_{ref} and m_{high} if $m_{\text{test}} > m_{\text{ref}}$.

When building the likelihood function three event classes are considered: signal, four-fermion background (including two-photon processes) and two-fermion background. The likelihood output gives the probability that a given event belongs to the signal rather than to one of the two background sources.

3.1 The two-jet plus tau final state

The analysis closely follows our published one at $\sqrt{s} = 183$ GeV [16]. It proceeds in two steps. First, events consistent with the final state topology of an isolated tau lepton, a pair of hadronic jets and sizable missing energy are preselected and are then processed by a likelihood selection. The sensitivity of the likelihood selection is improved by building mass-dependent discriminant functions as explained above.

Events are selected if their likelihood output (\mathcal{L}) is greater than a cut value chosen to maximize the sensitivity of the selection at each simulated charged Higgs-boson mass (m_{ref}). Apart from the neighborhood of the W^+W^- peak, the optimal cut does not depend significantly on the simulated mass and is chosen to be $\mathcal{L} > 0.85$. Around the W^+W^- peak, it is gradually reduced to 0.6.

The number of selected events per year is given in Table 2 for a test mass of $m_{H^{\pm}} = 75$ GeV. In total, 331 events are selected in the data sample with 316.9 \pm

Table 2 Observed data and expected SM background events for each year for the $2j + \tau$ and $4j$ final states. The uncertainty on the background prediction due to the limited number of simulated events is given

| LEP energy (year) | $2j + \tau$ | | $4j$ | |
|----------------------|-------------|-----------------|------|-----------------|
| | data | background | data | background |
| 189 GeV (1998) | 69 | 70.2 ± 1.6 | 309 | 338.9 ± 3.5 |
| 192–202 GeV (1999) | 103 | 96.1 ± 1.1 | 413 | 396.5 ± 2.3 |
| 203–209 GeV (2000) | 159 | 150.6 ± 2.7 | 378 | 382.4 ± 4.2 |

3.2 (stat.) ± 38.4 (syst.) events expected from SM processes. The sources of systematic uncertainties are discussed below. Four-fermion processes account for more than 99 % of the SM background and result in a large peak in the reconstructed mass centered at the W^\pm mass (with a second peak at the Z mass for test masses of $m_{H^\pm} > 85$ GeV). The signal detection efficiencies for the various LEP energies are between 25 % and 53 % for any charged Higgs-boson mass.

The likelihood output and reconstructed di-jet mass distributions for simulated Higgs-boson masses of 60 GeV and 75 GeV are presented in Figs. 1(a)–(d). The reconstructed Higgs-boson mass resolution is 2.0–2.5 GeV [16]. Figure 2(a) gives the mass dependence of the expected number of background and signal events and compares them to the observed number of events at each test mass.

The systematic uncertainties are estimated for several choices of the charged Higgs-boson mass from 50 GeV to 90 GeV at center-of-mass energies of $\sqrt{s} = 189$ GeV, 200 GeV and 206 GeV to cover the full LEP2 range. The following sources of uncertainties are considered: limited number of generated Monte Carlo events, statistical and systematic uncertainty on the luminosity measurement, modeling of kinematic variables in the preselection and in the likelihood selection, tau lepton identification, dependence of the signal detection efficiency on final-state quark flavor, signal selection efficiency interpolation between generated Monte Carlo points, background hadronization model, and four-fermion background model. The contributions from the different sources are summarized in Table 3.

In the limit calculation, the efficiency and background estimates of the $2j + \tau$ channel are reduced by 0.8–1.7 % (depending on the center-of-mass energy) in order to account for accidental vetoes due to accelerator-related backgrounds in the forward detectors.

3.2 The four-jet final state

The event selection follows our published analysis at $\sqrt{s} = 183$ GeV [16]: first, well-separated four-jet events with large visible energy are preselected; then a set of variables is combined using a likelihood technique. To improve the discriminating power of the likelihood selection, a new reference variable is introduced: the logarithm of the matrix element probability for W^+W^- production averaged over all possible jet-parton assignments computed by

EXCALIBUR [40]. Moreover, we introduce mass-dependent likelihood functions as explained above. As the optimal cut value on the likelihood output is not that sensitive to the charged Higgs-boson mass in this search channel, we use the condition $\mathcal{L} > 0.45$ at all center-of-mass energies and for all test masses.

There is a good agreement between the observed data and the SM Monte Carlo expectations at all stages of the selection. The number of selected events per year is given in Table 2 for a test mass of $m_{H^\pm} = 75$ GeV. In total, 1100 events are selected in the data, while 1117.8 ± 5.9 (stat.) ± 74.4 (syst.) events are expected from SM processes. The four-fermion processes account for about 90 % of the expected background and result in a large peak centered at the W^\pm mass and a smaller one at the Z boson mass. The signal detection efficiencies are between 41 % and 59 % for any test mass and center-of-mass energy.

Typical likelihood output and reconstructed di-jet mass distributions of the selected events together with the SM background expectation and signal shapes for simulated charged Higgs-boson masses of 60 GeV and 75 GeV are plotted in Figs. 1(e)–(h). The Higgs-boson mass can be reconstructed with a resolution of 1–1.5 GeV [16]. Figure 2(b) shows the mass dependence of the expected number of background and signal events and compares them to the observed number of events at each test mass. Systematic uncertainties are estimated in the same manner as for the $2j + \tau$ search and are given in Table 3.

4 Search for $AW^{+*}AW^{-*}$ events

In a large part of the 2HDM(I) parameter space, the branching ratio of $H^\pm \rightarrow AW^{\pm*}$ dominates. The possible decay modes of the A boson and the $W^{\pm*}$ lead to many possible $H^+H^- \rightarrow AW^{+*}AW^{-*}$ event topologies. Above $m_A \approx 12$ GeV, the A boson decays predominantly into a $b\bar{b}$ pair, and thus its detection is based on b-flavor identification. Two possibilities, covering 90 % of the decays of two $W^{\pm*}$, are considered: quark pairs from both $W^{\pm*}$ bosons or a quark pair from one and a leptonic final state from the other. The event topologies are therefore “eight jets” or “six jets and a lepton with missing energy”, with four jets containing b-flavor in both cases.

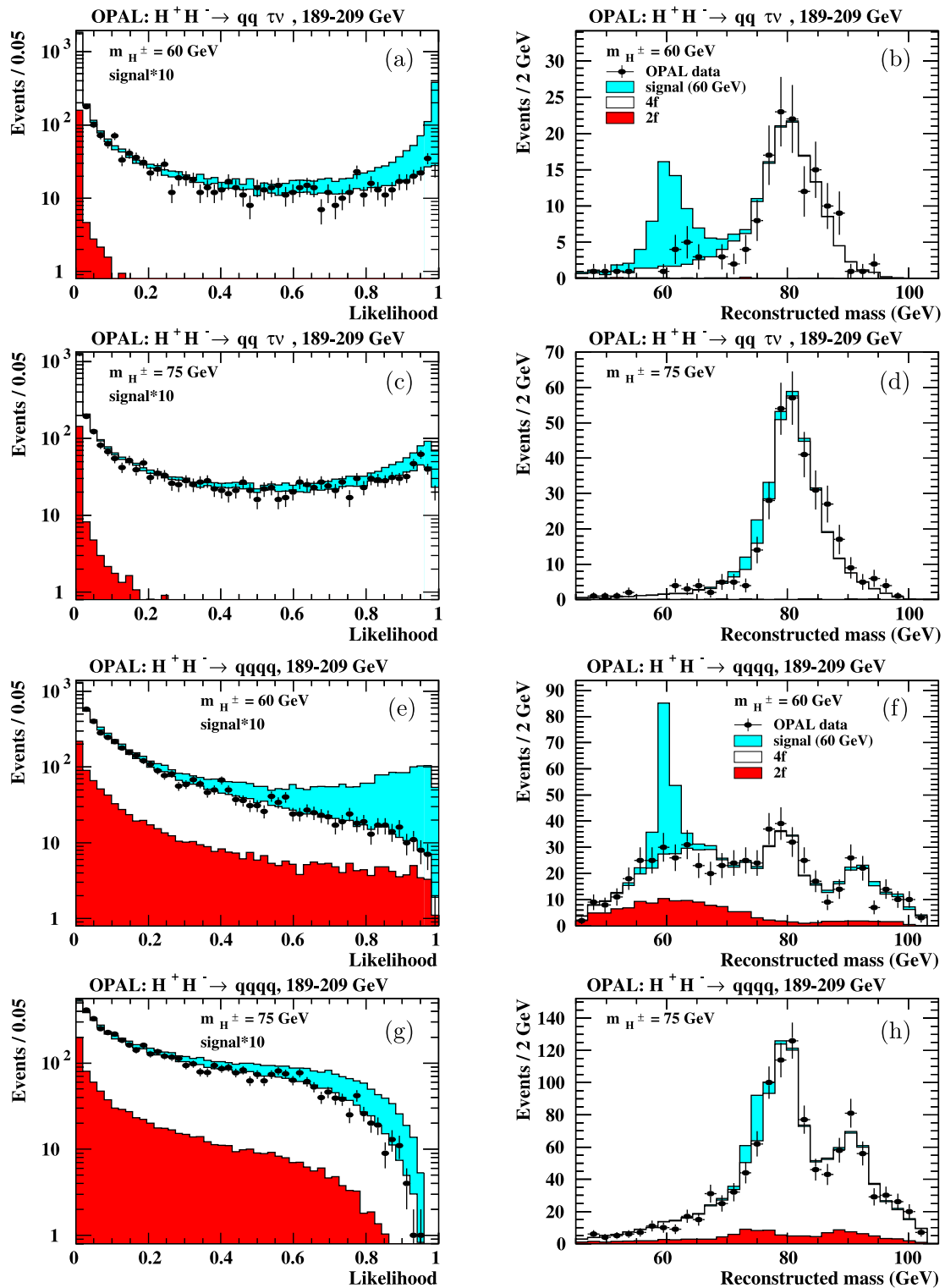


Fig. 1 Likelihood output and reconstructed di-jet mass distributions for the (a)–(d) $2j + \tau$ and (e)–(h) $4j$ channels. The distributions are summed up for all center-of-mass energies and correspond to 60 GeV and 75 GeV simulated charged Higgs-boson masses. All Monte Carlo distributions are normalized to the integrated luminosity of the data.

When plotting the likelihood output, the signal expectation is scaled up by a factor of 10 for better visibility. A hadronic branching ratio of 0.5 is assumed for the $2j + \tau$ signal, and 1.0 for the $4j$ signal. The reconstructed mass distributions are shown after the likelihood selection

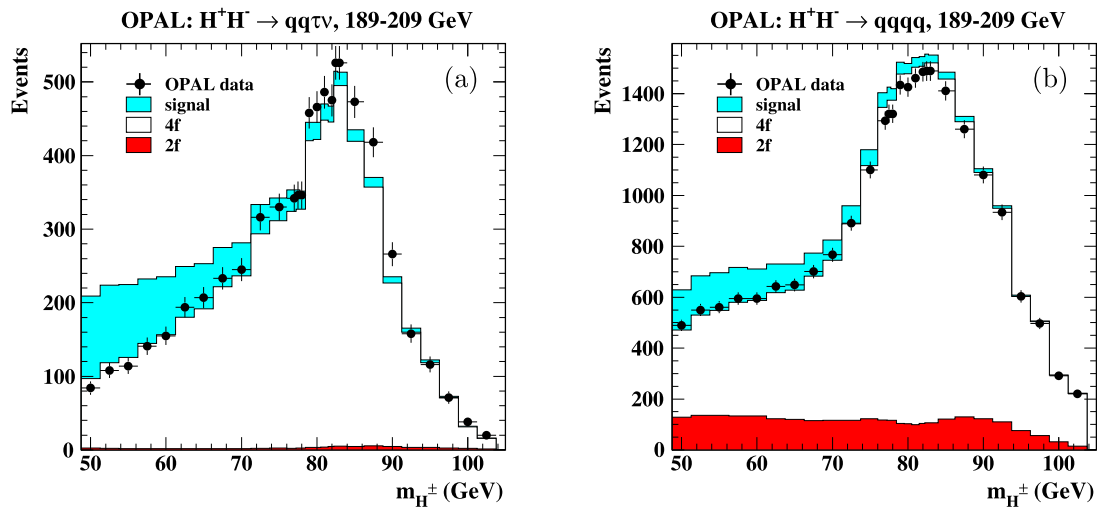


Fig. 2 The number of observed data, expected background and signal events for the (a) $2j + \tau$ and (b) $4j$ channels. The numbers are summed up for all center-of-mass energies and shown as a function of the reference charged Higgs-boson mass. A hadronic branching ratio of 0.5 is assumed for the $2j + \tau$ signal, and 1.0 for the $4j$ signal. Each bin

corresponds to a different likelihood selection optimized for the mass at which the dot is centered. Since the same background simulations are used to form the reference histograms and the same data enter the selection, the neighboring points are strongly correlated

Table 3 Relative systematic uncertainties on the expected background and signal rates for the $2j + \tau$ and $4j$ final states. The numbers are given in % and depend on the center-of-mass energy and the reference charged Higgs-boson mass. N.A. stands for not applicable, N. for negligible

| Source | $2j + \tau$ | | $4j$ | |
|----------------------|-------------|------------|---------|------------|
| | signal | background | signal | background |
| MC statistics | 3.1–4.6 | 1.4–4.3 | 1.6–2.4 | 0.9–1.9 |
| luminosity | 0.3 | 0.3 | 0.3 | 0.3 |
| preselection | 1.5–4.7 | 1.8–7.6 | 0.3–1.1 | 0.5–2.2 |
| likelihood selection | 0.9–6.5 | 5.8–22.7 | 0.7–2.4 | 2.1–7.5 |
| tau identification | 3.0 | 3.0 | N.A. | N.A. |
| quark flavor | 2.7–3.8 | N.A. | 1.2–6.4 | N.A. |
| interpolation | 0.2–0.4 | N.A. | 0.7–3.7 | N.A. |
| hadronization model | N. | 1.0–2.7 | N. | 0.7–4.1 |
| 4f background model | N.A. | 0.3–3.3 | N.A. | 1.7–3.7 |

The background comes from several Standard Model processes. ZZ and W^+W^- production can result in multi-jet events. While ZZ events can contain true b-flavored jets, W^+W^- events are selected as candidates when c-flavored jets fake b-jets. Radiative QCD corrections to $e^+e^- \rightarrow q\bar{q}$ also give a significant contribution to the expected background.

Due to the complexity of the eight-parton final state, it is more efficient to use general event properties and variables designed specifically to discriminate against the main background than a full reconstruction of the event. As a consequence, no attempt is made to reconstruct the charged Higgs-boson mass.

The analysis proceeds in two steps. First a preselection is applied to select b-tagged multi-jet events compatible with the signal hypothesis. Then a likelihood selection (with three

event classes: signal, four-fermion background and two-fermion background) is applied.

The preselection of multi-jet events uses the same variables as the search for the hadronic final state in [16] with optimized cut positions. However, it introduces a very powerful new criterion, especially against the W^+W^- background, on a combined b-tagging variable (\mathcal{B}_{evl}) requiring the consistency of the event with the presence of b-quark jets.

The neural network method used for b-tagging in the OPAL SM Higgs-boson search [24] is used to calculate on a jet-by-jet basis the discriminating variables $f_{c/b}^i$ and $f_{uds/b}^i$. These are constructed for each jet i as the ratios of probabilities for the jet to be c- or uds-like versus the probability to be b-like. The inputs to the neural network include information about the presence of secondary vertices in a jet, the jet shape, and the presence of leptons with large trans-

Table 4 Observed data and expected SM background events for each year in the $AW^{++}AW^{--}$ searches. The 8j and 6j + ℓ event samples after the preselection step (3rd and 4th columns) are highly overlapping. After the likelihood selection, the overlapping events are removed from

the 8j and 6j + ℓ samples and form a separate search channel (*last three columns*). The uncertainty on the background prediction due to the limited number of simulated events is given. The Monte Carlo reweighting to the measured gluon splitting rates is included

| LEP energy (year) | | Preselection 8j | Preselection 6j + ℓ | Exclusive 8j | Exclusive 6j + ℓ | Overlap |
|-----------------------|------------|--------------------|-----------------------------|-----------------|--------------------------|----------------|
| 189 GeV (1998) | data | 238 | 358 | 3 | 24 | 5 |
| | background | 231.2 ± 2.9 | 342.2 ± 3.6 | 2.1 ± 0.3 | 24.4 ± 1.0 | 6.3 ± 0.5 |
| 192–202 GeV (1999) | data | 297 | 310 | 16 | 16 | 17 |
| | background | 270.4 ± 2.9 | 285.0 ± 3.0 | 13.3 ± 0.7 | 10.4 ± 0.6 | 13.4 ± 0.7 |
| 200–209 GeV (2000) | data | 265 | 281 | 9 | 8 | 15 |
| | background | 252.5 ± 3.7 | 270.5 ± 5.0 | 13.0 ± 0.9 | 9.3 ± 0.8 | 12.9 ± 0.9 |

verse momentum. The Monte Carlo description of the neural network output was checked with LEP1 data with a jet energy of about 46 GeV. The main background in this search at LEP2 comes from four-fermion processes, in which the mean jet energy is about 50 GeV, very close to the LEP1 jet energy; therefore, an adequate modeling of the background is expected with the events reconstructed as four jets.

The $AW^{++}AW^{--}$ signal topology depends on the Higgs-boson masses. At $m_A \approx 12$ GeV or $m_A \approx m_{H^\pm}$, the available energy in the A or $W^{\pm*}$ system is too low to form two clean, collimated jets. At high m_{H^\pm} , the boost of the A and $W^{\pm*}$ bosons is small in the laboratory frame and the original eight partons cannot be identified. At low m_{H^\pm} , the A and $W^{\pm*}$ bosons might have a boost, but it is still not possible to resolve correctly the two partons from their decay. From these considerations, one can conclude that it is not useful to require eight (or even six) jets in the event, as these jets will not correspond to the original partons. Consequently, to get the best possible modeling of the background, four jets are reconstructed with the Durham jet-finding algorithm [46–49] before the b-tagger is run.

The flavor-discriminating variables are combined for the four reconstructed jets by

$$\mathcal{B}_{\text{evt}} = \frac{1}{1 + \alpha \cdot \prod_i f_{c/b}^i + \beta \cdot \prod_i f_{uds/b}^i}. \quad (1)$$

The index i runs over the reconstructed jets ($i = 1, \dots, 4$) and the parameters α and β are numerical coefficients whose optimal values depend on the flavor composition of the signal and background final states. However, since the expected sensitivity of the search is only slightly dependent on the values of α and β , they are fixed at $\alpha = 0.1$ and $\beta = 0.7$. Events are retained if $\mathcal{B}_{\text{evt}} > 0.4$.

The preselections of the two event topologies (8j and 6j + ℓ) are very similar. However, in the 6j + ℓ channel, no kinematic fit is made to the $W^+W^- \rightarrow q\bar{q}q\bar{q}$ hypothesis and, therefore, no cuts are made on the fit probabilities. No charged lepton identification is applied; instead the search

is based on indirect detection of the associated neutrino by measuring the missing energy.

After the preselection the observed data show an excess over the predicted Monte Carlo background. This can partly be explained by the apparent difference between the gluon splitting rate into $c\bar{c}$ and $b\bar{b}$ pairs in the data and in the background Monte Carlo simulation. The measured rates at $\sqrt{s} = 91$ GeV are $g_{c\bar{c}} = 3.2 \pm 0.21 \pm 0.38$ % [50] and $g_{b\bar{b}} = 0.307 \pm 0.053 \pm 0.097$ % [51] from the LEP1 OPAL data. The gluon splitting rates in our Monte Carlo simulation are extracted from $e^+e^- \rightarrow ZZ \rightarrow \ell^+\ell^-q\bar{q}$ events, where the $Z \rightarrow q\bar{q}$ decays have similar kinematic properties to the ones in the LEP1 measurement. Note that $e^+e^- \rightarrow ZZ \rightarrow q\bar{q}q\bar{q}$ events can not be used as the two $q\bar{q}$ pairs interact strongly with each other. The rates are found to be $g_{c\bar{c}}^{\text{MC}} = 1.33 \pm 0.06$ % and $g_{b\bar{b}}^{\text{MC}} = 0.116 \pm 0.0167$ %, averaged over all center-of-mass energies. This mismodeling can be compensated by reweighting the SM Monte Carlo events with gluon splitting to heavy quarks and at the same time doweighting the non-split events to keep the total numbers of W^+W^- , ZZ and two-fermion background events fixed at generator level. The reweighting factor is 2.41 for $g \rightarrow c\bar{c}$ and 2.65 for $g \rightarrow b\bar{b}$. The same reweighting factors are used for W^+W^- , ZZ and two-fermion events with gluon splitting at all LEP2 energies, noting that all background samples were hadronized with the same settings and assuming that the \sqrt{s} dependence of the gluon splitting of a fragmenting two-fermion system is correctly modeled by the Monte Carlo generator. It is known that the generator reproduces the energy dependence predicted by QCD in the order α_s with resummed leading-log and next-to-leading log terms [52]. This correction results in a background enhancement factor of 1.08 to 1.1 after the preselection, depending on the search channel and the center-of-mass energy, but it does not affect the shape of the background distributions.

The numbers of preselected events after the reweighting are given in columns 2 and 3 of Table 4. At this stage of the analysis the 8j and 6j + ℓ data samples are highly over-

lapping. The observed rates still show an excess over the background predictions, adding up to about 1.6 standard deviations in both samples. Although this difference is statistically not significant, it can be shown that the Monte Carlo prediction has minor imperfections. For the 8j case, the distributions of three variables used in the analysis, namely y_{34} , y_{56} and \mathcal{B}_{evt} , are plotted in the right part of Fig. 3. As can be seen, the variable y_{56} is most powerful to reject the background. Both the y_{34} and the y_{56} distributions are slightly shifted towards the position of a hypothetical Higgs signal and the \mathcal{B}_{evt} distribution shows an excess over the predicted background at intermediate \mathcal{B}_{evt} values, but the excess events are not distributed according to the expectation for a Higgs signal. The shifts are visible with better statistical significance in the left part of Fig. 3. It shows the same variables for a background enriched data sample, where the preselection cuts on y_{34} and \mathcal{B}_{evt} are dropped, except for the study of the y_{56} variable where we keep the cut on y_{34} to select multi-jet events. The resulting samples are completely dominated by background, the contribution of a Higgs signal being at most 0.5 %. Since heavy quark production in the Monte Carlo generator is already corrected, the origin of the discrepancies is likely a slight mismodeling of the topology of multi-jet events, especially if they contain heavy quarks. No further correction is applied to the estimated background. Excess events passing the final selection, even if they do not look signal-like, are thus counted with a certain weight as signal events in the statistical analysis, to be discussed later.

As a final selection, likelihood functions are built to identify signal events. The reference distributions depend on the LEP energy, but they are constructed to be independent of the considered (m_{H^\pm}, m_A) combination. To this end, we form the signal reference distributions by averaging all simulated H^+H^- samples in the (m_{H^\pm}, m_A) mass range of interest.

Since the selections at $\sqrt{s} = 192\text{--}209$ GeV are aimed at charged Higgs-boson masses around the expected sensitivity reach of about 80–90 GeV, all masses up to the kinematic limit are included. On the other hand, at $\sqrt{s} = 189$ GeV only charged Higgs-boson masses up to 50 GeV are included since the selections at this energy are optimized to reach down to as low as a charged Higgs-boson mass of 40 GeV where the LEP1 exclusion limit lies. The input variables for the 8j final state are: the Durham jet-resolution parameters² $\log_{10} y_{34}$ and $\log_{10} y_{56}$, the oblateness [53] event shape variable, the opening angle of the widest jet defined by the size of the cone containing 68 % of the total jet energy, the cosine of the W production angle multiplied with the W charge (calculated from the jet

charges [54]) for the $e^+e^- \rightarrow W^+W^- \rightarrow q\bar{q}q\bar{q}$ interpretation, and the b-tagging variable \mathcal{B}_{evt} . At $\sqrt{s} = 189$ GeV, $\log_{10} y_{23}$, $\log_{10} y_{45}$, $\log_{10} y_{67}$, and the maximum jet energy are also used. Moreover, the sphericity [55] event shape variable has more discriminating power and thus replaces oblateness. Although the y_{ij} variables are somewhat correlated, they contain additional information: their differences reflect the kinematics of the initial partons.

The input variables for the 6j + ℓ selection are: $\log_{10} y_{34}$, $\log_{10} y_{56}$, the oblateness, the missing energy of the event, and \mathcal{B}_{evt} . At $\sqrt{s} = 189$ GeV, $\log_{10} y_{23}$, the maximum jet energy and the sphericity are also included.

Events are selected if they pass a lower cut on the likelihood output. The likelihood distributions are shown in Fig. 4. The positions of the likelihood cuts are indicated by vertical lines. The discrepancies observed in Fig. 3 in background-enriched samples, propagate into the likelihood distributions. Since the excess events in Fig. 3 are shifted relative to the background expectation, but do not agree with the Higgs distribution, they give likelihood values between the mean background and signal values in Fig. 4. With large statistical errors, the effect can be seen at intermediate likelihood values. Some of the excess events pass the final likelihood cut.

To assure that every event is counted only once in the final analysis, the overlapping 8j and 6j + ℓ event samples, as obtained after the final likelihood cut are redistributed into three event classes: (i) events exclusively classified as 8j candidates, (ii) events exclusively classified as 6j + ℓ candidates and (iii) events accepted by both selections. If an event falls into class (iii), the larger likelihood output of the two selections is kept for further processing. The final results using the above classification are quoted in Table 4. After all selection cuts, an excess of events appears in the 1999 data sample. The excess (1.9σ) is not statistically significant and it is consistent with the results of the other years. This modified channel definition not only removes the overlap but also increases the efficiency for detecting signal events by considering the cross-channel efficiencies (e.g. the efficiency to select $H^+H^- \rightarrow b\bar{b}q\bar{q}b\bar{b}q\bar{q}$ signal by the exclusive 6j + ℓ selection can be as high as 18 %, though it is typically only a few %). The efficiencies are determined independently for all simulated (m_{H^\pm}, m_A) combinations and interpolated to arbitrary (m_{H^\pm}, m_A) by two-dimensional spline interpolation. The behavior of the selection efficiencies depends strongly on the targeted charged Higgs-boson mass range and also varies with the mass difference $\Delta m = m_{H^\pm} - m_A$. In most cases the overlap channel has the highest efficiency. At $\sqrt{s} = 189$ GeV and $m_{H^\pm} = 45$ GeV, it reaches 32 % for the $b\bar{b}q\bar{q}b\bar{b}q\bar{q}$ and 44 % for the $H^+H^- \rightarrow b\bar{b}q\bar{q}b\bar{b}q\bar{q}$ signal. At $\sqrt{s} = 206$ GeV and $m_{H^\pm} = 90$ GeV, the overlap efficiency can be as high as 62 % for the $b\bar{b}q\bar{q}b\bar{b}q\bar{q}$ and 71 % for the $H^+H^- \rightarrow b\bar{b}q\bar{q}b\bar{b}q\bar{q}$ signal. The exclusive 6j + ℓ se-

²Throughout this paper y_{ij} denotes the parameter of the Durham jet finder at which the event classification changes from i -jet to j -jet, where $j = i + 1$.

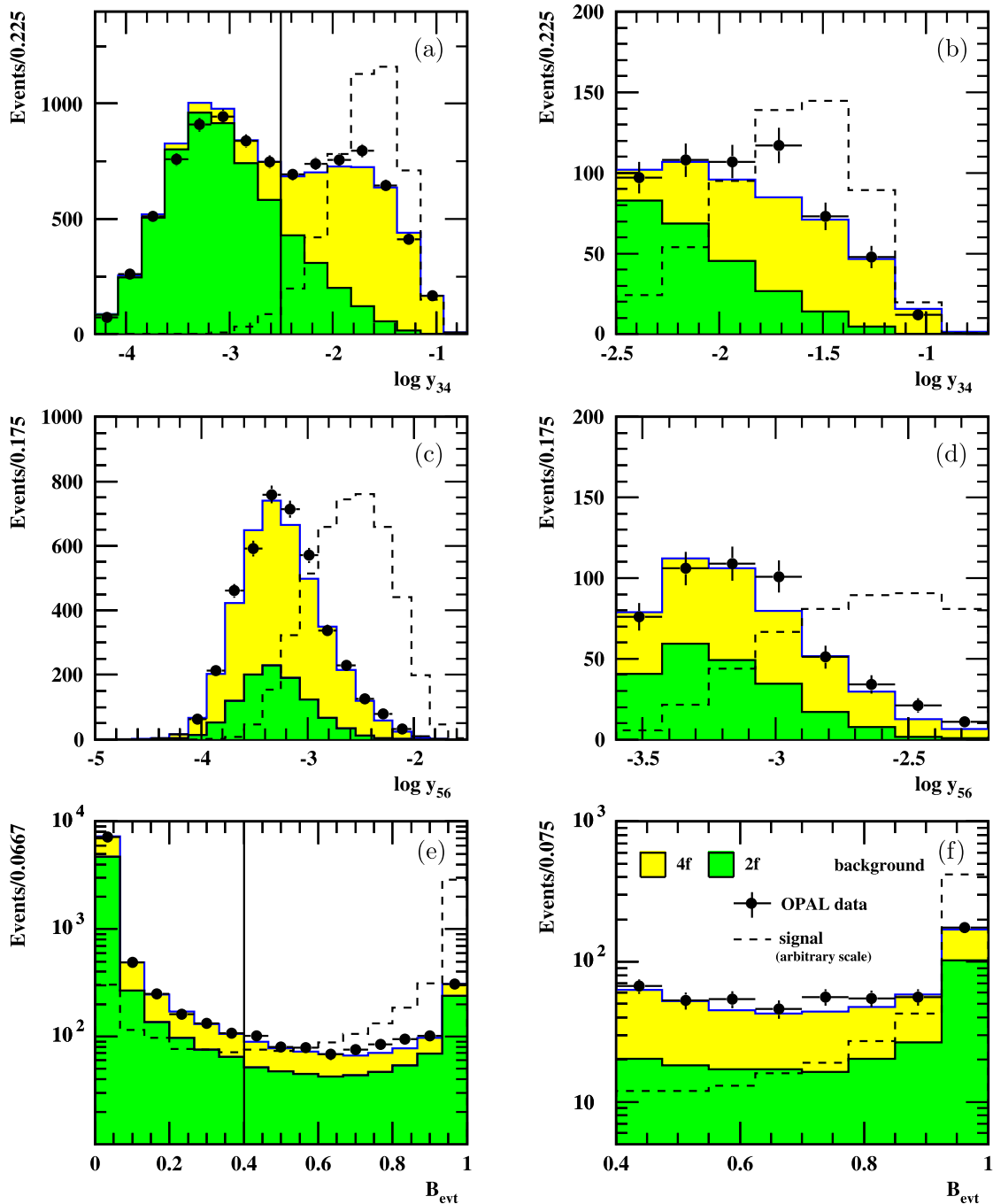
OPAL: $H^+H^- \rightarrow bbqqbbqq$, 192–209 GeV

Fig. 3 Most important selection variables: (a)–(b) $\log_{10} y_{34}$, (c)–(d) $\log_{10} y_{56}$ and (e)–(f) B_{evt} in the 8j channel at $\sqrt{s} = 192\text{--}209$ GeV. The distributions are shown (left) in a background-enriched data sample (see text for explanation) and (right) after the full preselection. To form the signal histograms, the Monte Carlo distributions are averaged

for all simulated (m_{H^\pm}, m_A) mass combinations in the mass range of interest. The Monte Carlo reweighting to the measured gluon splitting rates is included. The expectations from SM processes are normalized to the data luminosity. The preselection cuts on y_{34} and B_{evt} are indicated by vertical lines

lection has efficiencies typically below 20–30 %, while the exclusive 8j selection below 10–15 %. Table 5 gives the selection efficiencies at selected (m_{H^\pm}, m_A) points.

The composition of the background depends on the targeted Higgs-boson mass region. In the low-mass selection ($\sqrt{s} = 189$ GeV) that is optimized for $m_{H^\pm} = 40\text{--}50$ GeV,

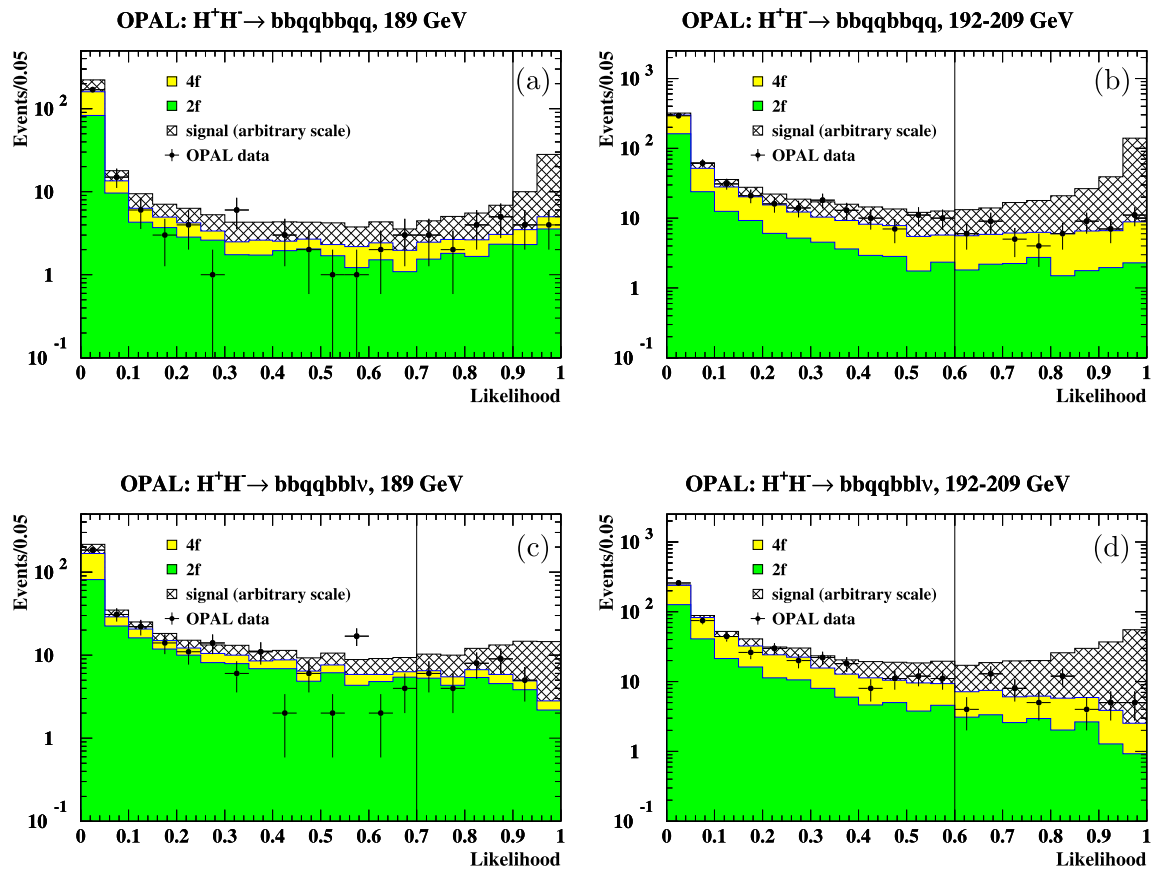


Fig. 4 Likelihood output distributions for the (a)–(b) 8j and (c)–(d) 6j + ℓ channels at $\sqrt{s} = 189$ GeV and 192–209 GeV. To form the signal histograms, the Monte Carlo distributions are averaged for all simulated (m_{H^\pm}, m_A) mass combinations in the mass range of interest.

The Monte Carlo reweighting to the measured gluon splitting rates is included. The expectations from SM processes are normalized to the data luminosity. The lower cuts on the likelihood output are indicated by vertical lines

Table 5 Signal selection efficiencies in percent for the $H^\pm \rightarrow AW^{\pm*}$ final states in the different search channels at $\sqrt{s} = 189$ and 206 GeV at representative (m_{H^\pm}, m_A) points

| Signal | Selection | (m_{H^\pm}, m_A) (GeV, GeV) | | | |
|--|-------------|-------------------------------|----------|----------------------|----------|
| | | $\sqrt{s} = 189$ GeV | | $\sqrt{s} = 206$ GeV | |
| | | (45, 30) | (80, 50) | (45, 30) | (90, 60) |
| $b\bar{b}q\bar{q}b\bar{b}q\bar{q}$ | 8j | 4.6 | 1.0 | 9.3 | 12.4 |
| | overlap | 41.0 | 2.8 | 14.9 | 69.6 |
| | 6j + ℓ | 17.0 | 3.6 | 4.1 | 3.1 |
| | total | 62.6 | 7.4 | 28.3 | 85.0 |
| $b\bar{b}q\bar{q}b\bar{b}\ell\nu_\ell$ | 6j + ℓ | 28.2 | 6.0 | 11.6 | 7.0 |
| | overlap | 31.8 | 3.6 | 14.2 | 62.2 |
| | 8j | 1.8 | 0.1 | 2.2 | 6.1 |
| | total | 61.8 | 9.7 | 28.0 | 75.3 |
| $b\bar{b}q\bar{q}\tau\nu_\tau$ | 4j + τ | 68.0 | 0.0 | 12.3 | 11.1 |

the Higgs bosons are boosted and therefore the final state is two-jet-like with the largest background contribution coming from two-fermion processes: they account for 52 % in the exclusive 8j, 80 % in the exclusive 6j + ℓ and 76 % in

the overlap channel. On the other hand, in the high-mass analysis ($\sqrt{s} = 192$ –209 GeV) the four-fermion fraction is dominant: 69 % in the 8j, 56 % in the 6j + ℓ and 70 % in the overlap channel.

Table 6 Relative systematic uncertainties in percent for the $AW^{\pm*}AW^{-*}$ searches. Where two values are given separated by a “/”, the first belongs to the 189 GeV selection and the second to the 192–209 GeV selections. For the signal, the uncertainties due to the limited Monte Carlo statistics are calculated by binomial statistics for a sample

size of 500 events and they also depend, via the selection efficiency, on the assumed Higgs-boson masses. N.A. stands for not applicable. The multiplicative gluon splitting correction factors, used to obtain the background-rate estimates as explained in the text, are given in the last line

| Source | Exclusive 8j | | Exclusive 6j + ℓ | | Overlap | |
|-----------------------------------|--------------------|------------|-----------------------|------------|---------------------|------------|
| | signal | background | signal | background | signal | background |
| MC statistics | $\geq 15/\geq 8.5$ | 13.2/6.7 | $\geq 5.7/\geq 8.4$ | 4.0/8.3 | $\geq 4.0/\geq 2.8$ | 7.9/7.1 |
| Preselection | 1.0 | 1.0 | 1.0 | 2.0 | 1.0 | 2.0/1.5 |
| \mathcal{L} selection | | | | | | |
| y_{ij} | 4.0/1.8 | 6.0/6.2 | 2.2/2.6 | 6.0/8.0 | 2.8/1.5 | 5.5/4.9 |
| b-tag | 0.0/1.8 | 4.7/7.0 | 2.9/1.4 | 4.4/7.1 | 1.0/1.3 | 4.0/5.1 |
| other | 1.8/0.7 | 3.9/3.2 | 1.0/1.6 | 3.7/3.5 | 1.2/0.7 | 3.4/2.4 |
| Gluon splitting | | | | | | |
| $g \rightarrow c\bar{c}$, exp. | N.A. | 0.6/2.5 | N.A. | 1.6 | N.A. | 1.4/2.3 |
| $g \rightarrow c\bar{c}$, MC | N.A. | 0.2/0.8 | N.A. | 0.6 | N.A. | 0.5/0.8 |
| $g \rightarrow b\bar{b}$, exp. | N.A. | 1.4/4.2 | N.A. | 3.8/4.3 | N.A. | 5.5/5.4 |
| $g \rightarrow b\bar{b}$, MC | N.A. | 0.5/1.7 | N.A. | 1.5/1.7 | N.A. | 2.2 |
| Gluon splitting correction factor | N.A. | 1.05/1.18 | N.A. | 1.13/1.15 | N.A. | 1.15/1.22 |

Systematic errors arise from uncertainties in the preselection and from mismodeling of the likelihood function. The variables y_{34} and \mathcal{B}_{evt} appear both in the preselection cuts and in the likelihood definition. The total background rate is known to be underestimated after the preselection step. The computation of upper limits on the production cross section, with this background rate subtracted, results in conservative limits, assuming the modeling of the other preselection variables and the signal and background likelihoods to be correct. Therefore, no systematic uncertainty is assigned to the percentage of events passing the y_{34} and \mathcal{B}_{evt} preselection cuts. The systematic errors related to preselection variables other than y_{34} and \mathcal{B}_{evt} , evaluated from background enriched data samples, are taken into account.

As already mentioned, the discrepancies shown in Fig. 3 have an impact on the likelihood function. Event-by-event correction routines for the variables y_{34} and \mathcal{B}_{evt} were developed to describe the observed shapes, keeping the normalization above the preselection cuts fixed. The systematic errors were estimated by computing the likelihood for all MC events with the modified values of y_{34} and \mathcal{B}_{evt} and counting the accepted MC events. The systematic errors related to all other reference variables were estimated in the same manner.

Systematic uncertainties also arise due to the gluon splitting correction. The experimental uncertainty on the gluon splitting rate translates into uncertainties on the total back-

ground rates. Moreover, there is an uncertainty due to the Monte Carlo statistics of the $g \rightarrow c\bar{c}$ and $b\bar{b}$ events.

Finally, uncertainties due to the limited number of simulated signal and background events are included. The different contributions are summarized in Table 6. Uncertainties below the 1 % level are neglected.

5 Search for $AW^{\pm*}\tau\nu_\tau$ events

In some parts of the 2HDM(I) parameter space, both the fermionic $H^\pm \rightarrow \tau\nu_\tau$ and the bosonic $H^\pm \rightarrow AW^{\pm*}$ decay modes contribute. To cover this transition region at small $m_{H^\pm} - m_A$ mass differences, a search for the final state $H^+H^- \rightarrow AW^{\pm*}\tau\nu_\tau$ is performed. The transition region is wide for small $\tan\beta$ and narrow for large $\tan\beta$; therefore, this analysis is more relevant for lower values of $\tan\beta$.

Only the hadronic decays of $W^{\pm*}$ and the decay $A \rightarrow b\bar{b}$ are considered. Thus the events contain a tau lepton, four jets (two of which are b-flavored) and missing energy. Separating the signal from the W^+W^- background becomes difficult close to $m_{H^\pm} = m_{W^\pm}$.

The preselection is designed to identify hadronic events containing a tau lepton plus significant missing energy and transverse momentum from the undetected neutrino. In most cases it is not practical to reconstruct the four jets originating from the $AW^{\pm*}$ system. Instead, to suppress the main background from semi-leptonic W^+W^- events, we remove the decay products of the tau candidate and force the remaining

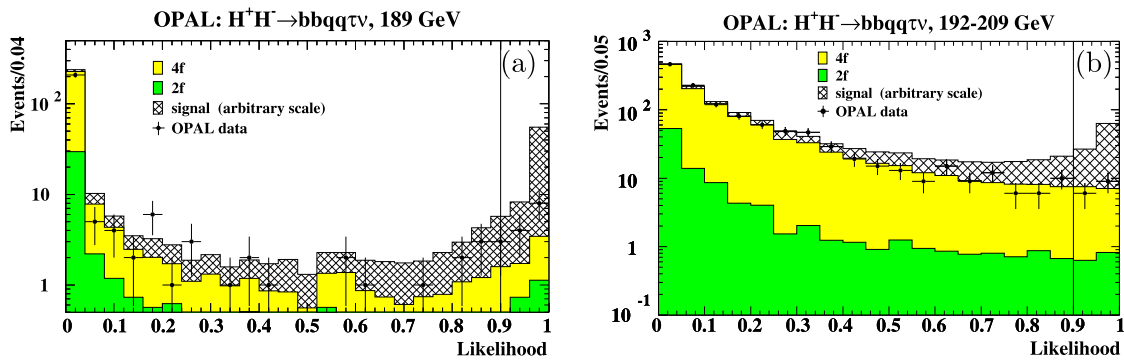


Fig. 5 Likelihood output distribution for the $4j + \tau$ channel at (a) $\sqrt{s} = 189$ GeV and (b) $\sqrt{s} = 192\text{--}209$ GeV. To form the signal histograms, the Monte Carlo distributions are averaged for all simu-

lated (m_{H^\pm}, m_A) mass combinations in the mass range of interest. The expectations from SM processes are normalized to the data luminosity. The lower cuts on the likelihood output are indicated by vertical line

hadronic system into two jets by the Durham algorithm. The requirements are then based on the preselection of Sect. 3.1 with additional preselection cuts on the effective center-of-mass energy, $\log_{10} y_{12}$ and $\log_{10} y_{23}$ of the hadronic system, and the charge-signed W^\pm production angle.

The likelihood selection uses seven variables: the momentum of the tau candidate, the cosine of the angle between the tau momentum and the nearest jet, $\log_{10} y_{12}$ of the hadronic system, the cosine of the angle between the two hadronic jets, the charge-signed cosine of the W^\pm production angle, the invariant mass of the hadronic system, and the b-tagging variable \mathcal{B}_{evt} . Here, \mathcal{B}_{evt} is defined using the two jets of the hadronic system using Eq. (1) of Sect. 4, with $i = 1, 2$ and $\alpha = \beta = 1$. To form the signal reference distributions, all simulated H^+H^- samples in the (m_{H^\pm}, m_A) mass range of interest are summed up. Since the search at $\sqrt{s} = 192\text{--}209$ GeV targets intermediate charged Higgs-boson masses (60–80 GeV), all masses up to the kinematic limit are included. At $\sqrt{s} = 189$ GeV, only charged Higgs-boson masses up to 50 GeV are included since the selection is optimized for low charged Higgs-boson masses (40–50 GeV).

The likelihood output distributions are shown in Fig. 5. There is an overall agreement between data and background distributions, apart from a small discrepancy at 189 GeV. Events are selected if their likelihood output is larger than 0.9. In total, 15 data events survive the selection at $\sqrt{s} = 192\text{--}209$ GeV, to be compared with 14.8 ± 0.6 (stat.) ± 1.9 (syst.) events expected from background sources. At $\sqrt{s} = 189$ GeV, where the selection is optimized for low Higgs-boson masses, 13 data events are selected with 6.1 ± 0.5 (stat.) ± 1.3 (syst.) events expected. The contribution of four-fermion events, predominantly from semi-leptonic W^+W^- production, amounts to 67 % at $\sqrt{s} = 189$ GeV and to 90 % at $\sqrt{s} = 192\text{--}209$ GeV.

At $\sqrt{s} = 192\text{--}209$ GeV, the signal selection efficiency starts at about 5 % at $m_{H^\pm} = 40$ GeV, reaches its maximum of about 40 % (depending on the mass difference

Table 7 Systematic uncertainties in percent for the $4j + \tau$ channel. Where two values are given separated by a “/”, the first one belongs to the 189 GeV selection and the second to the 192–209 GeV selections. For the signal, the uncertainties due to the limited Monte Carlo statistics are calculated by binomial statistics for a sample size of 500 events and they also depend, via the selection efficiency, on the assumed Higgs-boson masses

| Source | $4j + \tau$ | |
|-----------------------|---------------------|------------|
| | signal | background |
| MC statistics | $\geq 2.7/\geq 4.5$ | 8.2/7.0 |
| Preselection: | tau ID | 0.0 |
| | other | 0.0/1.0 |
| Likelihood selection: | b-tag | 0.3/1.4 |
| | other | 3.2/2.1 |
| | | 18.4/11.2 |

$\Delta m = m_{H^\pm} - m_A$) at $m_{H^\pm} = 60$ GeV, then decreases to 12 % at $m_{H^\pm} = 90$ GeV. In the low-mass selection at $\sqrt{s} = 189$ GeV, the efficiency depends strongly on the mass difference: at $m_{H^\pm} = 40$ GeV, it is 27 % for $\Delta m = 2.5$ GeV and 60 % for $\Delta m = 10$ GeV. The selection efficiency approaches its maximum at $m_{H^\pm} = 50$ GeV (73 % for $\Delta m = 15$ GeV) and then drops to zero at $m_{H^\pm} = 80$ GeV. Table 5 gives selection efficiencies at representative (m_{H^\pm}, m_A) points.

The systematic uncertainties due to the modeling of selection variables are evaluated with the method developed for the $AW^{+*}AW^{-*}$ channels and summarized in Table 7.

6 Interpretation

None of the searches has revealed a signal-like excess over the SM expectation. The results presented here and those published previously [16, 44] by the OPAL Collaboration

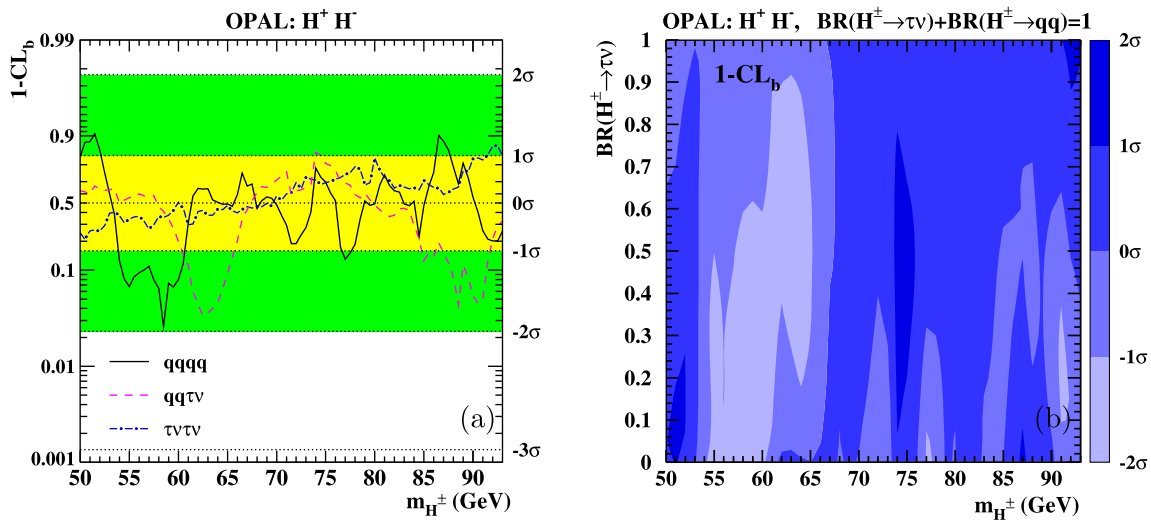


Fig. 6 The observed confidence levels for the background interpretation of the data, $1 - CL_b$, (a) for the three different final states as a function of the charged Higgs-boson mass, and (b) for the combined

result in 2HDM(II) assuming $BR(H^\pm \rightarrow \tau \nu_\tau) + BR(H^\pm \rightarrow q\bar{q}) = 1$ on the $[m_{H^\pm}, BR(H^\pm \rightarrow \tau \nu_\tau)]$ plane. The significance values corresponding to the different shadings are shown by the bar at the right

Table 8 Discriminating variables entering the statistical analysis for each search topology. Previously published results are also included

| Channel | \sqrt{s} (GeV) | Discriminant |
|-------------|------------------|---------------------------|
| 2τ | 183 | simple event counting |
| 2τ | 189–209 | likelihood output |
| $2j + \tau$ | 183–209 | reconstructed di-jet mass |
| $4j$ | 183–209 | reconstructed di-jet mass |
| $8j$ | 189 | simple event counting |
| $8j$ | 192–209 | likelihood output |
| $6j + \ell$ | 189 | simple event counting |
| $6j + \ell$ | 192–209 | likelihood output |
| $4j + \tau$ | 189–209 | simple event counting |

are combined using the method of [56] to study the compatibility of the observed events with “background-only” and “signal plus background” hypotheses and to derive limits on charged Higgs-boson production. The statistical analysis is based on weighted event counting, with the weights computed from physical observables, also called discriminating variables of the candidate events (see Table 8). Systematic uncertainties with correlations are taken into account in the confidence level (p -value) calculations. To improve the sensitivity of the analysis, they are also incorporated into the weight definition [56].³

³For the weight definition, we use criteria (i) and (ii) in the 2HDM parameter scans and criterion (vii) in calculating model independent results. The generalized version of Eq. (2.9), given in Eq. (6.1), is used to include systematic errors in the event weights. The treatment of correlations between systematic errors is discussed in Sect. 5.1.

The results are interpreted in two different scenarios: in the traditional, supersymmetry-favored 2HDM(II) (assuming that there are no new additional light particles other than the Higgs bosons) and in the 2HDM(I) where under certain conditions fermionic couplings are suppressed.

First, we calculate $1 - CL_b$, the confidence [56] under the background-only hypothesis, and then proceed to calculate limits on the charged Higgs-boson production cross section in the signal + background hypothesis. These results are used to provide exclusions in the model parameter space, and in particular, on the charged Higgs-boson mass.

6.1 2HDM type II

First a general 2HDM(II) is considered, where $BR(H^\pm \rightarrow \tau \nu_\tau) + BR(H^\pm \rightarrow q\bar{q}) = 1$. This model was thoroughly studied at LEP. It is realized in supersymmetric extensions of the SM if no new additional light particles other than the Higgs bosons are present. As our previously published mass limit in such a model is $m_{H^\pm} > 59.5$ GeV [16], only charged Higgs-boson masses above 50 GeV are tested. Cross-section limits for lower masses can be found in [15]. In this model, the results of the 2τ , $2j + \tau$ and $4j$ searches enter the statistical combination.

The confidence $1 - CL_b$ is plotted for each channel separately in Fig. 6(a) and combined in Fig. 6(b). Note that $1 - CL_b < 0.5$ translates to negative values of sigma (as indicated by the dual y-axis scales in Fig. 6(a)) and indicates an excess of events. No deviation reaches the 2σ level.

The results are used to set upper bounds on the charged Higgs-boson pair production cross section relative to the 2HDM prediction as calculated by HZHA. The limits ob-

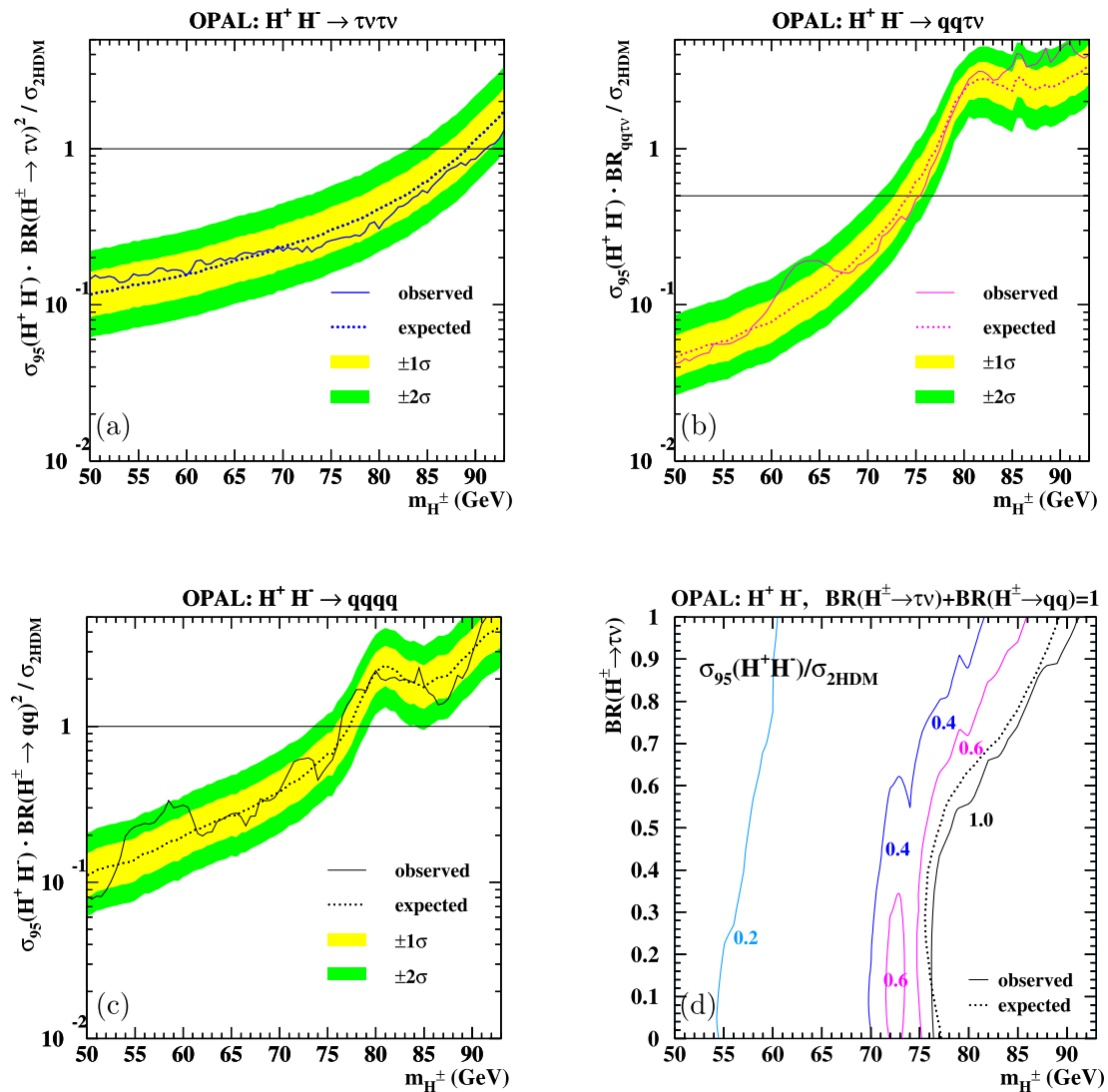


Fig. 7 Observed and expected 95 % CL upper limits on the $H^+ H^-$ production cross section times the relevant H^\pm decay branching ratios relative to the theoretical prediction for the (a) $\tau \nu \tau \nu$ (b) $qq\tau\nu$ and (c) $qq\bar{q}\bar{q}$ channels. The horizontal lines indicate the maximum possible branching ratios for a given channel. In (b), $BR_{qq\tau\nu} = 2 \cdot BR(H^\pm \rightarrow$

$\tau \nu_\tau) \cdot BR(H^\pm \rightarrow q\bar{q})$. (d) Upper limits on the production cross section relative to the 2HDM prediction on the $[m_{H^\pm}, BR(H^\pm \rightarrow \tau \nu_\tau)]$ plane in 2HDM(II) assuming $BR(H^\pm \rightarrow \tau \nu_\tau) + BR(H^\pm \rightarrow q\bar{q}) = 1$. The plotted curves are isolines along which the observed limit is equal to the number indicated

tained are shown for each channel separately in Figs. 7(a)–(c) and combined in Fig. 7(d). The combined results are shown by “isolines” along which $\sigma_{95}(H^+ H^-)/\sigma_{2HDM}$, the ratio of the limit on the production cross section and the 2HDM cross-section prediction, is equal to the number indicated next to the curves.

Excluded areas on the $[m_{H^\pm}, BR(H^\pm \rightarrow \tau \nu_\tau)]$ plane are presented for each channel separately in Fig. 8(a) and combined in Fig. 8(b). The expected mass limit from simulated background experiments, assuming no signal, is also shown. For the combined results, the 90 % and 99 % CL contours are also given. Charged Higgs bosons are excluded up to a mass of 76.3 GeV at 95 % CL, independent of

$BR(H^\pm \rightarrow \tau \nu_\tau)$. Lower mass limits for different values of $BR(H^\pm \rightarrow \tau \nu_\tau)$ are presented in Table 9.

6.2 2HDM type I

We present here for the first time an interpretation of the OPAL charged Higgs-boson searches in an alternative theoretical scenario, a 2HDM(I). The novel feature of this model with respect to the more frequently studied 2HDM(II) is that the fermionic decays of the charged Higgs boson can be suppressed. If the A boson is light, the $H^\pm \rightarrow AW^{\pm*}$ decay may play a crucial role.

The charged Higgs-boson sector in these models is described by three parameters: m_{H^\pm} , m_A and $\tan \beta$. To test this

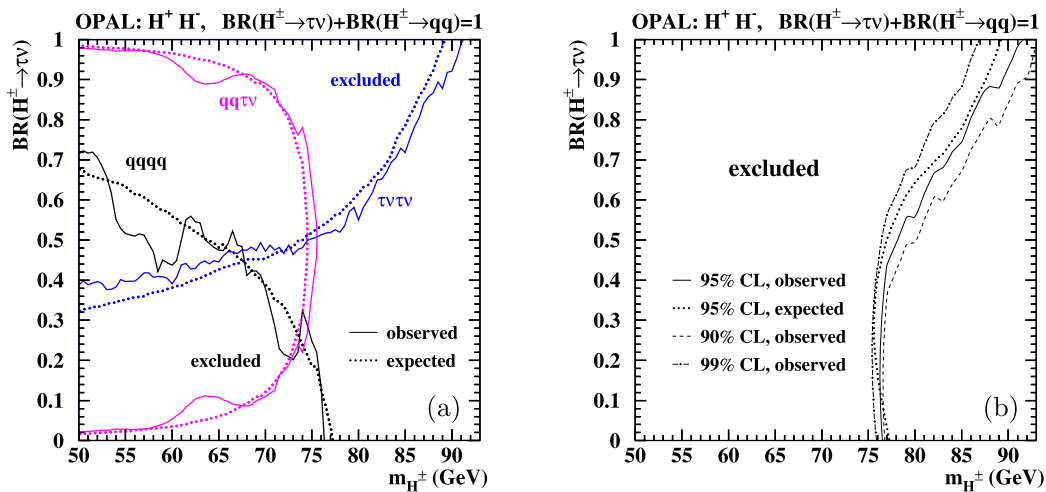


Fig. 8 Observed and expected excluded areas at 95 % CL on the $[m_{H^\pm}, BR(H^\pm \rightarrow \tau \nu_\tau)]$ plane (a) for each search channel separately and (b) combined in 2HDM(II) assuming $BR(H^\pm \rightarrow \tau \nu_\tau) + BR(H^\pm \rightarrow qq) = 1$

Table 9 Observed and expected lower limits at 95 % CL on the mass of the charged Higgs boson in 2HDM(II) assuming $BR(H^\pm \rightarrow \tau \nu_\tau) + BR(H^\pm \rightarrow q\bar{q}) = 1$. For the results independent of the branching ratio (last line), the $BR(H^\pm \rightarrow \tau \nu_\tau)$ value at which the limit is set, is given in parenthesis

| $BR(H^\pm \rightarrow \tau \nu_\tau)$ | Lower mass limit (GeV) | |
|---------------------------------------|------------------------|-------------|
| | Observed | Expected |
| 0 | 76.5 | 77.2 |
| 0.5 | 78.3 | 77.0 |
| 0.65 | 81.9 | 80.5 |
| 1 | 91.3 | 89.2 |
| any | 76.3 (0.15) | 75.6 (0.27) |

scenario, the Higgs-boson decay branching ratios $H^\pm \rightarrow \tau \nu_\tau$, $c\bar{s}$, $c\bar{b}$, $AW^{\pm*}$ and $A \rightarrow b\bar{b}$ are calculated by the program of Akeroyd et al. [13, 14], and the model parameters are scanned in the range: $40 \text{ GeV} \leq m_{H^\pm} \leq 94 \text{ GeV}$, $12 \text{ GeV} \leq m_A < m_{H^\pm}$, $0 \leq \tan \beta \leq 100$. Charged Higgs-boson pair production is excluded below 40 GeV by the measurement of the Z boson width [57]. As the A boson detection is based on the identification of b-quark jets, no limits are derived for $m_A < 2m_b$.

Both the fermionic (2τ , $2j + \tau$ and $4j$) and the bosonic ($4j + \tau$, $6j + \ell$ and $8j$) final states play an important role and therefore their results have to be combined. There is, however, a significant overlap between the events selected by the $H^+H^- \rightarrow q\bar{q}q\bar{q}$ and $H^+H^- \rightarrow AW^{\pm*}AW^{\mp*}$ selections, and the events selected by the $H^+H^- \rightarrow q\bar{q}\tau\nu_\tau$ and $H^+H^- \rightarrow AW^{\pm*}\tau\nu_\tau$ selections. Therefore, an automatic procedure is implemented to switch off the less sensitive of the overlapping channels, based on the calculation of the expected limit

$BR(H^\pm \rightarrow q\bar{q}) = 1$. For the combined result, the 90 % and 99 % CL observed limits are also shown. See Table 9 for numerical values of the combined limit

assuming no signal. In general the fermionic channels are used close to the (m_{H^\pm}, m_A) diagonal and for low $\tan \beta$, and the searches for $H^\pm \rightarrow AW^{\pm*}$ are crucial for low values of m_A and high values of $\tan \beta$.

The confidence $1 - CL_b$ is calculated for the combination of the $8j$ and $6j + \ell$ searches and for the $4j + \tau$ search, without requiring the 2HDM(I) branching ratios (model independent scan), and for $\tan \beta$ dependent combinations of all channels, including the fermionic ones, taking the 2HDM(I) cross section predictions into account (model dependent scan).

The result for the $8j$ and $6j + \ell$ combination is calculated assuming SM branching ratios [58] for the $W^{\pm*}$ decay and is shown in Fig. 9(a). Close to the (m_{H^\pm}, m_A) diagonal, the eight- or six-jet structure of a $H^\pm \rightarrow AW^{\pm*}$ signal becomes less pronounced and the final state turns out four-jet-like with a few soft extra particles. As the selection variables for the signal and the background become similar, the likelihood cut removes more signal events, resulting in a drop in efficiency and extrapolations towards the $m_{H^\pm} = m_A$ limit are unreliable. Moreover, within the 2HDM(I), the branching ratio for the bosonic Higgs decay vanishes at $m_{H^\pm} = m_A$. Results for $m_A > m_{H^\pm} - 3 \text{ GeV}$ are thus not included in Fig. 9(a). In this mass region, the branching ratios for both $H^+H^- \rightarrow 8j$ and $H^+H^- \rightarrow 6j + \ell$ are always less than 10^{-4} . The largest deviation from background expectation, $1 - CL_b = 0.029$, corresponding to 1.9σ is reached at $m_{H^\pm} = 70 \text{ GeV}$ and $m_A = 64 \text{ GeV}$. Another local minimum at $m_{H^\pm} = 60 \text{ GeV}$ and $m_A = 12 \text{ GeV}$, not visible in Fig. 9(a), has $1 - CL_b = 0.052$. However, the mean background shift on the $[m_{H^\pm}, m_A]$ plane amounts only to 1.1σ .

The $1 - CL_b$ values for the $4j + \tau$ channel is shown in Fig. 9(b). Mass combinations with $m_A > m_{H^\pm} - 2.5 \text{ GeV}$

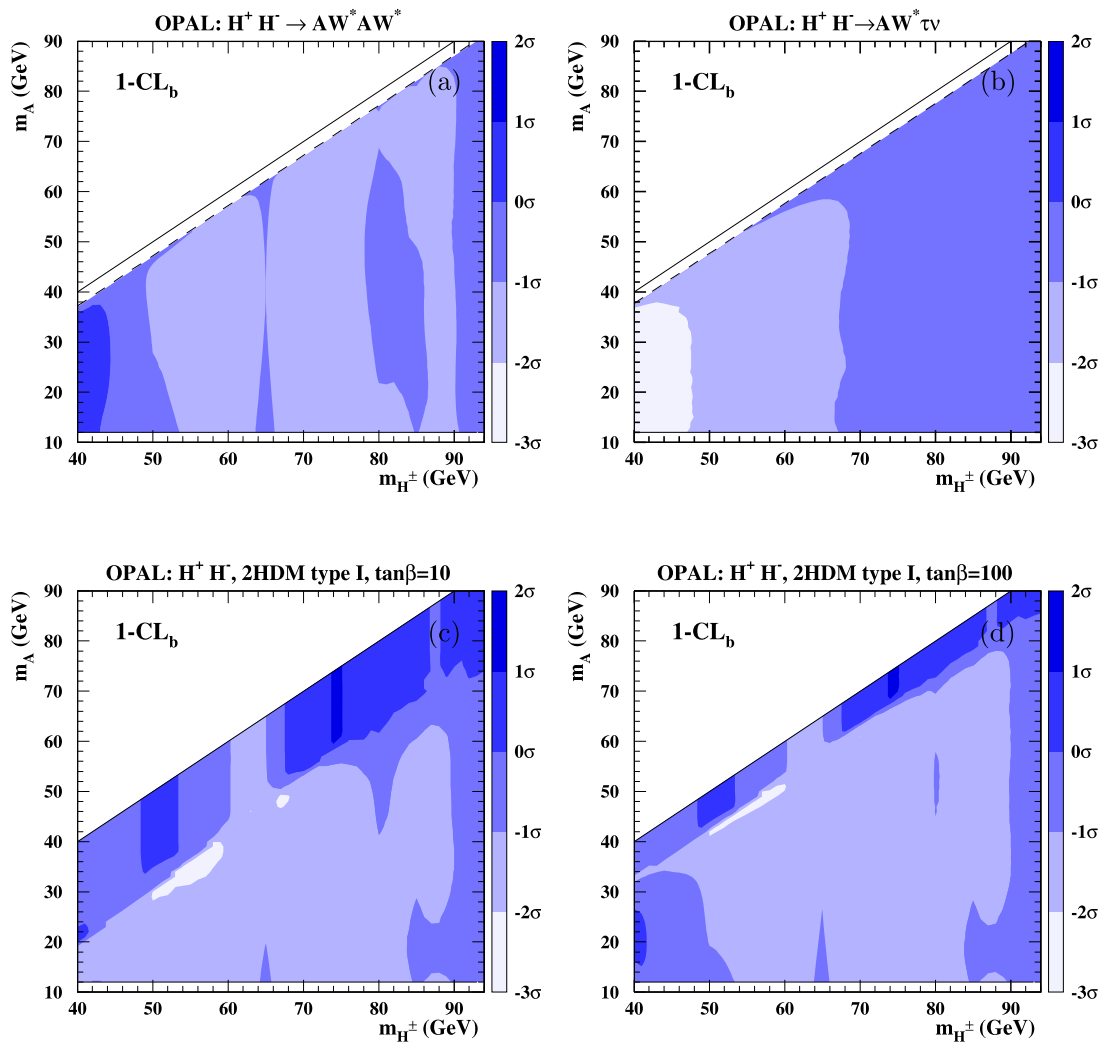


Fig. 9 The confidence $1 - CL_b$ on the $[m_{H^\pm}, m_A]$ plane (a) for $H^+H^- \rightarrow AW^{**}AW^{*-}$ combining the results of the $6j + \ell$ and $8j$ searches, and (b) for $H^+H^- \rightarrow AW^{\pm*}\tau\nu_\tau$ from the $4j + \tau$ search. The

combined results in 2HDM(I) for (c) $\tan\beta = 10$ and (d) $\tan\beta = 100$ are also shown. The significance values corresponding to the different shadings are shown by the bars at the right

are not included. In this mass region, the 2HDM(I) prediction for the $H^+H^- \rightarrow 4j + \tau$ branching ratio is less than 0.005. The largest deviation $1 - CL_b = 0.013$ corresponding to 2.2σ appears for low charged Higgs-boson masses ($m_{H^\pm} = 40$ GeV, $m_A = 21$ GeV), reflecting the excess of events in the $\sqrt{s} = 189$ GeV search. The mean background shift for this channel is 0.8σ .

When all channels are combined within the 2HDM(I), the confidence levels shown in Figs. 9(c)–(d) are obtained. Close to the (m_{H^\pm}, m_A) diagonal, the results are determined by the analysis of the fermionic channels. The 2HDM(I) predicts $BR(H^\pm \rightarrow \tau\nu_\tau) \approx 0.65$ for the branching ratio, depending only weakly on m_{H^\pm} . The upper parts of Figs. 9(c)–(d) correspond thus to an almost horizontal cut in Fig. 6(b) at $BR(H^\pm \rightarrow \tau\nu_\tau) = 0.65$. The lower parts of Figs. 9(c)–(d) are essentially weighted combinations of the results in

Figs. 9(a)–(b), depending on $\tan\beta$ and the masses involved. However, it has to be noted that also the decays $H^+H^- \rightarrow \tau^+\nu_\tau\tau^-\bar{\nu}_\tau$ are included and that the event weights in the statistical analysis are somewhat different for the model independent scans in Figs. 9(a)–(b) and the model dependent scans in Figs. 9(c)–(d). In general, excesses in Figs. 9(a)–(b) add up to excesses less than 2σ in the combination. A few regions with a significance above 2σ are present. For $\tan\beta = 10$, the largest excess $1 - CL_b = 0.014$, corresponding to 2.2σ , is found at $m_{H^\pm} = 55$ GeV and $m_A = 34$ GeV (just before switching from the bosonic to the fermionic channels). This excess corresponds to a signal rate of 28.5 % of the 2HDM(I) expectation. Noting that the event weights depend on the hypothetical signal rate, structures in the $1 - CL_b$ distribution as a function of $\Delta m = m_{H^\pm} - m_A$ are due to the similar increase of the signal cross-section with

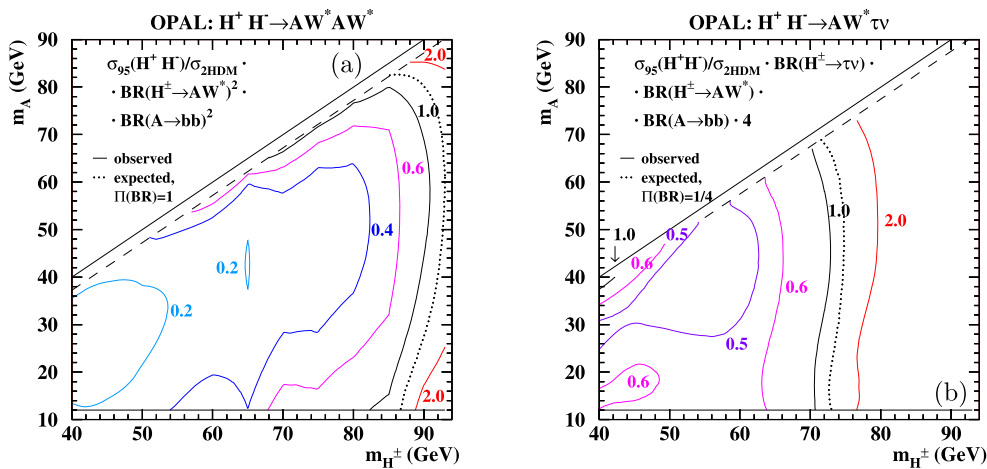


Fig. 10 The 95 % CL upper limits on the production cross section times relevant H^\pm and A boson decay branching ratios relative to the 2HDM prediction on the $[m_{H^\pm}, m_A]$ plane for the process (a) $H^+H^- \rightarrow AW^{+*}AW^{-*}$ and (b) $H^+H^- \rightarrow AW^{+*}\tau\nu_\tau$. The plotted curves are isolines along which the observed limit is

equal to the number indicated. The expected limits are given for (a) $BR(H^\pm \rightarrow AW^{\pm*})^2 \cdot BR(A \rightarrow b\bar{b})^2 = 1$ and (b) $BR(H^\pm \rightarrow \tau\nu_\tau) \cdot BR(H^\pm \rightarrow AW^{\pm*}) \cdot BR(A \rightarrow b\bar{b}) = 0.25$ corresponding to the maximal value in 2HDM(I). Please note that the plotted quantity on (b) is scaled by 4 to take into account this maximal branching fraction

Table 10 Lower mass limits for the charged Higgs boson in 2HDM(I). For the $\tan\beta \leq 100$ results, the $\tan\beta$ value at which the limit is set is indicated in parenthesis. For any $\tan\beta$ value, an extrapolation of the exclusion limits to $m_{H^\pm} = m_A$ gives the result quoted in Table 9 for $BR(H^\pm \rightarrow \tau\nu_\tau) = 0.65$

| $\tan\beta$ | m_A | Limit on m_{H^\pm} (GeV) | |
|-------------|--|----------------------------|------------|
| | | observed | expected |
| ≤ 100 | $12 \text{ GeV} \leq m_A \leq m_{H^\pm}$ | 56.8 (3.5) | 71.1 (1.0) |
| | $m_A = 12 \text{ GeV}$ | 56.8 (3.5) | 71.1 (1.0) |
| | $m_A = m_{H^\pm}/2$ | 66.1 (3.5) | 73.9 (1.5) |
| | $m_A \geq m_{H^\pm} - 10 \text{ GeV}$ | 65.0 (100) | 71.9 (100) |
| | $m_A \geq m_{H^\pm} - 5 \text{ GeV}$ | 80.3 (100) | 77.3 (100) |
| ≤ 0.1 | $12 \text{ GeV} \leq m_A \leq m_{H^\pm}$ | 81.6 | 80.0 |
| | $m_A = 12 \text{ GeV}$ | 81.6 | 80.0 |
| | $m_A = m_{H^\pm}/2$ | 81.8 | 80.4 |
| | $m_A \geq m_{H^\pm} - 10 \text{ GeV}$ | 81.9 | 80.5 |
| | $m_A \geq m_{H^\pm} - 5 \text{ GeV}$ | 81.9 | 80.5 |
| 1 | $12 \text{ GeV} \leq m_A \leq m_{H^\pm}$ | 66.5 | 71.1 |
| | $m_A = 12 \text{ GeV}$ | 66.5 | 71.1 |
| | $m_A = m_{H^\pm}/2$ | 78.3 | 76.6 |
| | $m_A \geq m_{H^\pm} - 10 \text{ GeV}$ | 81.9 | 80.5 |
| | $m_A \geq m_{H^\pm} - 5 \text{ GeV}$ | 81.9 | 80.5 |
| 10 | $12 \text{ GeV} \leq m_A \leq m_{H^\pm}$ | 65.9 | 73.8 |
| | $m_A = 12 \text{ GeV}$ | 69.0 | 82.8 |
| | $m_A = m_{H^\pm}/2$ | 86.6 | 89.5 |
| | $m_A \geq m_{H^\pm} - 10 \text{ GeV}$ | 81.3 | 79.4 |
| | $m_A \geq m_{H^\pm} - 5 \text{ GeV}$ | 81.8 | 80.4 |
| 100 | $12 \text{ GeV} \leq m_A \leq m_{H^\pm}$ | 65.0 | 71.9 |
| | $m_A = 12 \text{ GeV}$ | 69.4 | 82.9 |
| | $m_A = m_{H^\pm}/2$ | 87.1 | 89.8 |
| | $m_A \geq m_{H^\pm} - 10 \text{ GeV}$ | 65.0 | 71.9 |
| | $m_A \geq m_{H^\pm} - 5 \text{ GeV}$ | 80.3 | 77.4 |

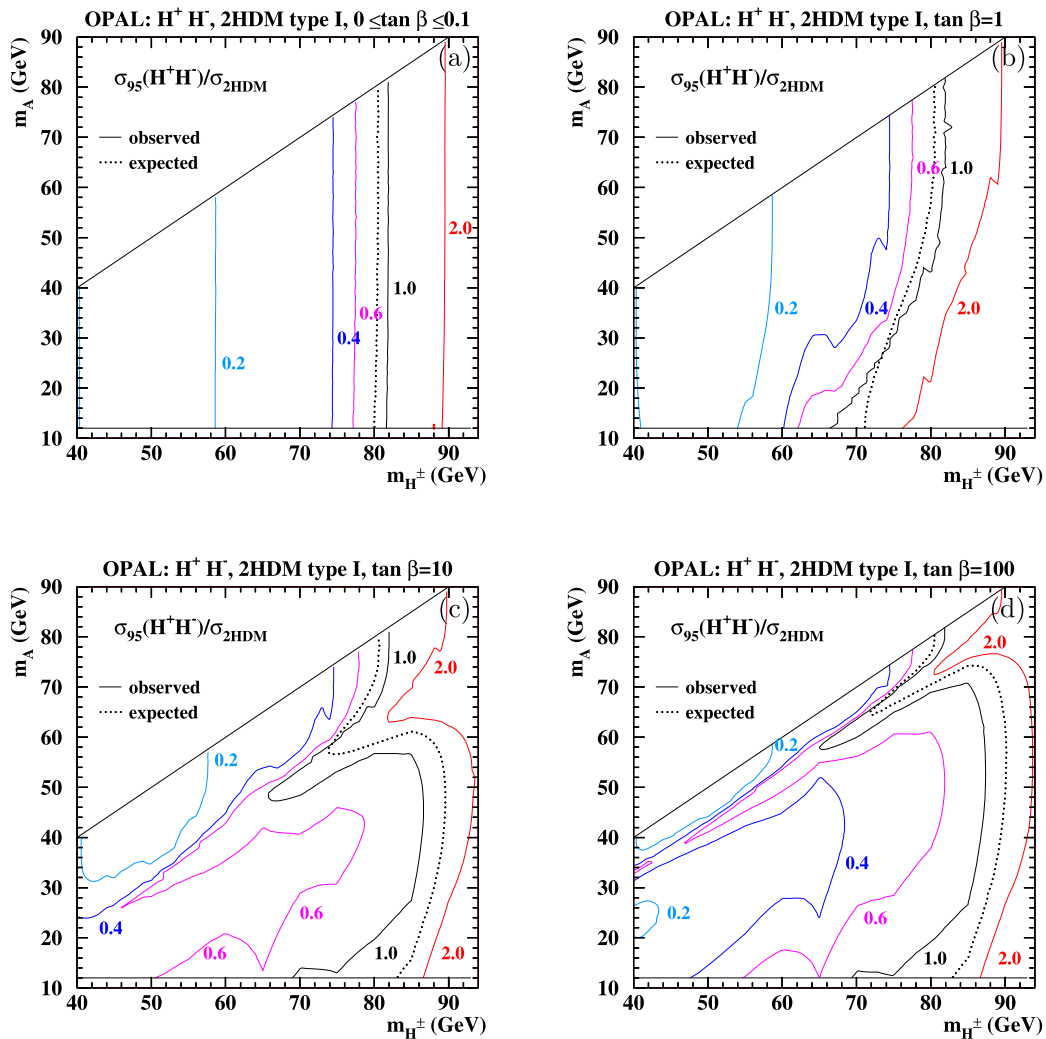


Fig. 11 The 95 % CL upper limits on the production cross section in 2HDM(I) relative to the theoretical prediction on the $[m_{H^\pm}, m_A]$ plane for different choices of $\tan\beta$: (a) 0.1, (b) 1.0, (c) 10.0 and (d) 100.0.

Δm for different m_{H^\pm} values. The rise of the cross-section is steeper for larger $\tan\beta$, therefore the low $1 - CL_b$ region shrinks from Fig. 9(c) to Fig. 9(d).

In the limit of small m_A and large values of $\tan\beta$, the Higgs decay into the $\tau\nu_\tau$ channel is suppressed. The structures of the $1 - CL_b$ bands close to $m_A = 12$ GeV in Figs. 9(a) and 9(d) are therefore very similar.

As mentioned previously, the $H^\pm \rightarrow AW^{\pm*}$ decay becomes dominant if the A boson is sufficiently light. The smaller $\tan\beta$ is, the smaller m_A should be. This is clearly seen from the structure of the result in Figs. 9(c)–(d): for $\tan\beta = 10$, the bosonic decay becomes dominant at $m_A \lesssim m_{H^\pm} - 18$ GeV, while for $\tan\beta = 100$, it dominates already at $m_A \lesssim m_{H^\pm} - 6$ GeV.

The model-independent limits on the charged Higgs-boson production cross section relative to the 2HDM predic-

The plotted curves are isolines along which the observed limit is equal to the number indicated

tion are presented in Fig. 10(a) for the $H^+H^- \rightarrow AW^{\pm*}AW^{\mp*}$ and in Fig. 10(b) for $H^+H^- \rightarrow AW^{\pm*}\tau\nu_\tau$ searches, with the only assumption that $W^{\pm*}$ decays with SM branching ratios. The exclusion line for 40 % of the total production cross section in Fig. 10(a) forms an island around $m_{H^\pm} = 60$ GeV and $m_A = 12$ GeV, corresponding to the minimum of $1 - CL_b$ at this point.

The results combining all channels using 2HDM(I) branching ratios are shown in Fig. 11 for different choices of $\tan\beta$. For $0 \leq \tan\beta \leq 0.1$, the excluded mass region is independent of m_A , since the $AW^{\pm*}$ final state does not contribute. The Higgs mass limit is identical to the 2HDM(II) limit at $\text{BR}(H^\pm \rightarrow \tau\nu_\tau) = 0.65$. This limit is also reached at the (m_{H^\pm}, m_A) diagonal for any value of $\tan\beta$. For intermediate and large values of $\tan\beta$, the boundary lines of the excluded mass regions have two local m_{H^\pm} minima. The

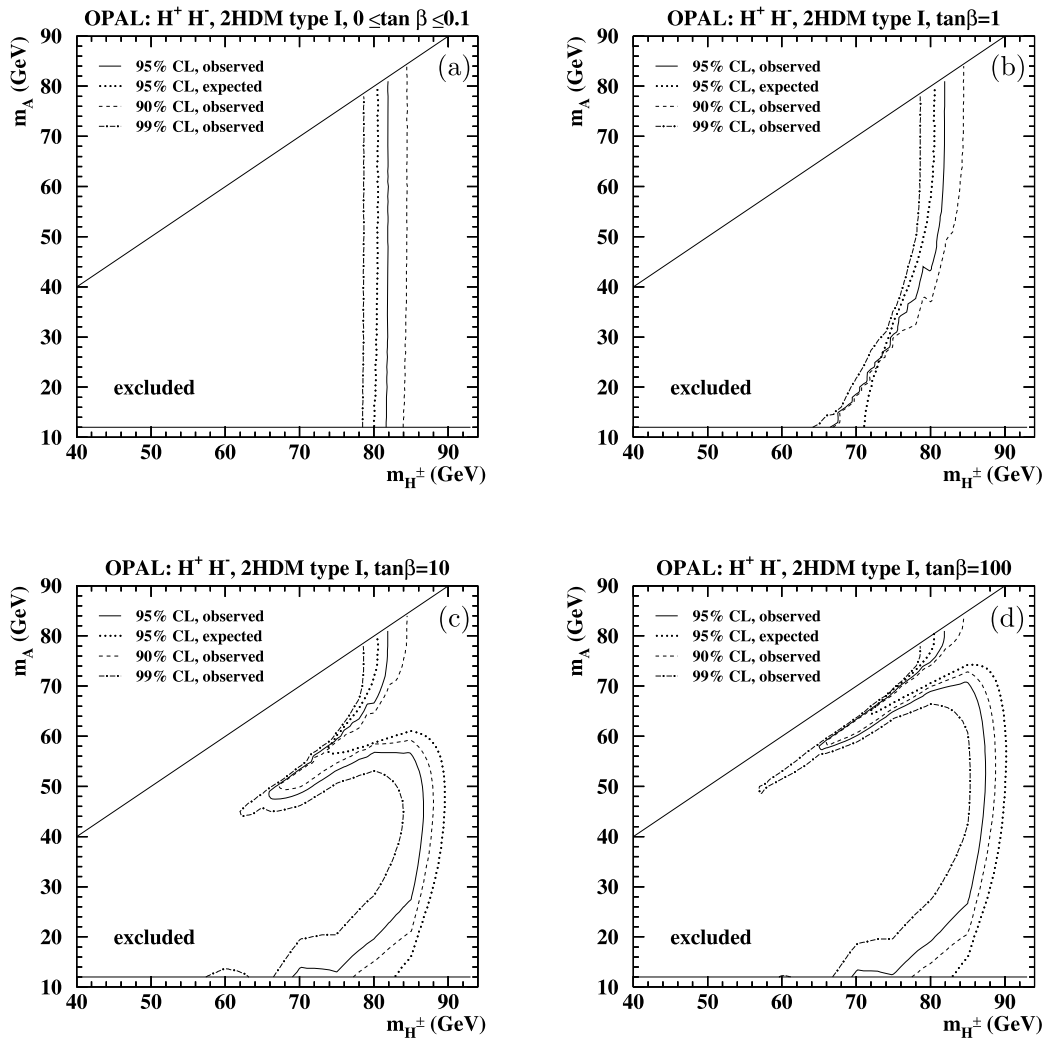


Fig. 12 Excluded areas at 90 %, 95 % and 99 % CL on the $[m_{H^\pm}, m_A]$ plane in 2HDM(I) for different choices of $\tan\beta$: (a) 0.1, (b) 1.0, (c) 10.0 and (d) 100.0

first minimum at $m_A = 12$ GeV is due to the excess of events in the $AW^{+*}AW^{-*}$ searches. The second minimum is at a region extending parallel to the (m_{H^\pm}, m_A) diagonal (see the full and dotted black curves corresponding to a cross-section ratio of 1.0). This reflects the loss of sensitivity in the $AW^{+*}AW^{-*}$ searches for mass combinations without a pronounced $8j$ or $6j + \ell$ structure and is also due to the channel switching procedure implemented to avoid the use of overlapping events as explained above.

To further study the behavior of the unexcluded regions, 90 %, 95 % and 99 % CL excluded areas are shown in Fig. 12 for different choices of $\tan\beta$. The island at $m_{H^\pm} = 60$ GeV can not be excluded at the 99 % CL.

Due to the excess of events in the $H^+H^- \rightarrow AW^{+*}AW^{-*}$ searches in the year 1999 data, the observed limit is lower than the expectation in all regions where the $H^\pm \rightarrow AW^{\pm*}$ decay dominates. Our final results are presented, for all

$\tan\beta$, in Fig. 13, and the limits on charged Higgs-boson mass are summarized in Table 10. Since an excess is present in both the $8j$ and $6j + \ell$ combination and the $4j + \tau$ channel, and the relative weighting of these channels depends on $\tan\beta$, the size of the mentioned island is $\tan\beta$ dependent. The absolute lower limit on the charged Higgs boson mass for 95 % CL is set by $\tan\beta = 3.5$, as indicated in Fig. 13. It amounts to 56.8 GeV for $0 \leq \tan\beta \leq 100$ and $12 \text{ GeV} \leq m_A \leq m_{H^\pm}$, to be compared with an expectation of 71.1 GeV. The unexcluded island is no longer present at 90 % CL where the observed mass limit improves to 66.0 GeV.

For $m_A > 15$ GeV, the $\tan\beta$ -independent lower limit on the charged Higgs-boson mass at 95 % CL is 65.0 GeV with 71.3 GeV expected. The limit is found in the transition region where the bosonic and fermionic channels have comparable sensitivities. The 6 GeV difference is due to the excess observed in the $H^+H^- \rightarrow AW^{+*}AW^{-*}$ search.

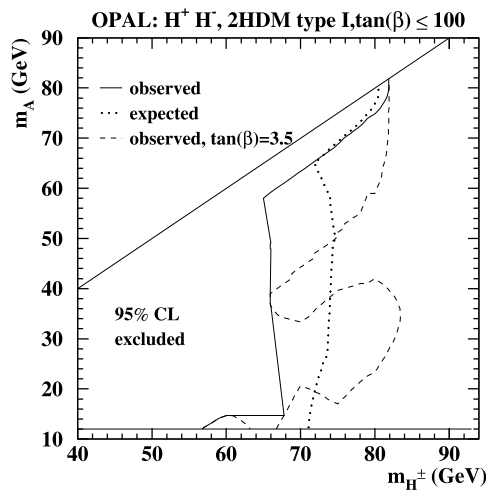


Fig. 13 Excluded areas in 2HDM(I) on the $[m_{H^\pm}, m_A]$ plane independent of $\tan \beta$ at 95 % CL. The weakest overall mass limit is defined by the $\tan \beta = 3.5$ exclusion, which is also shown

7 Summary

A search is performed for the pair production of charged Higgs bosons in electron-positron collisions at LEP2, considering the decays $H^\pm \rightarrow \tau \nu_\tau$, $q\bar{q}$ and $AW^{\pm*}$. No signal is observed. The results are interpreted in the framework of Two-Higgs-Doublet Models.

In 2HDM(II), required by the minimal supersymmetric extension of the SM, charged Higgs bosons are excluded up to a mass of 76.3 GeV (with an expected limit of 75.6 GeV) when $\text{BR}(H^\pm \rightarrow \tau \nu_\tau) + \text{BR}(H^\pm \rightarrow q\bar{q}) = 1$ is assumed. $\text{BR}(H^\pm \rightarrow \tau \nu_\tau)$ -dependent limits are given in Fig. 8 and Table 9.

In 2HDM(I), where fermionic decays can be suppressed and $H^\pm \rightarrow AW^{\pm*}$ can become dominant, a $\tan \beta$ -independent lower mass limit of 56.8 GeV is observed for $m_A > 12$ GeV (with an expected limit of 71.1 GeV) due to an excess observed at $\sqrt{s} = 192\text{--}202$ GeV in the $H^+H^- \rightarrow AW^{\pm*}AW^{\mp*}$ search, discussed in Sect. 4. For $m_A > 15$ GeV, the observed limit improves to $m_{H^\pm} > 65.0$ GeV (with an expected limit of 71.3 GeV). Figure 13 shows the excluded areas in the $[m_{H^\pm}, m_A]$ plane and Table 10 reports selected numerical results.

Acknowledgements We particularly wish to thank the SL Division for the efficient operation of the LEP accelerator at all energies and for their close cooperation with our experimental group. In addition to the support staff at our own institutions we are pleased to acknowledge the Department of Energy, USA, National Science Foundation, USA, Particle Physics and Astronomy Research Council, UK, Natural Sciences and Engineering Research Council, Canada, Israel Science Foundation, administered by the Israel Academy of Science and Humanities, Benozio Center for High Energy Physics,

Japanese Ministry of Education, Culture, Sports, Science and Technology (MEXT) and a grant under the MEXT International Science Research Program,

Japanese Society for the Promotion of Science (JSPS), German Israeli Bi-national Science Foundation (GIF), Bundesministerium für Bildung und Forschung, Germany, National Research Council of Canada, Hungarian Foundation for Scientific Research, OTKA T-038240, and T-042864, The NWO/NATO Fund for Scientific Research, the Netherlands.

Open Access This article is distributed under the terms of the Creative Commons Attribution License which permits any use, distribution, and reproduction in any medium, provided the original author(s) and the source are credited.

References

1. S.L. Glashow, Nucl. Phys. **22**, 579 (1961)
2. S. Weinberg, Phys. Rev. Lett. **19**, 1264 (1967)
3. A. Salam, in *Elementary Particle Theory*, ed. by N. Svartholm (Almqvist and Wiksells, Stockholm, 1968), 367 pp.
4. P.W. Higgs, Phys. Lett. **12**, 132 (1964)
5. F. Englert, R. Brout, Phys. Rev. Lett. **13**, 321 (1964)
6. G.S. Guralnik, C.R. Hagen, T.W.B. Kibble, Phys. Rev. Lett. **13**, 585 (1964)
7. J.F. Gunion, H.E. Haber, G.L. Kane, S. Dawson, *The Higgs Hunter's Guide* (Addison-Wesley, Reading, 1990); and references therein
8. S.L. Glashow, S. Weinberg, Phys. Rev. D **15**, 1977 (1958)
9. E.A. Paschos, Phys. Rev. D **15**, 1977 (1966)
10. H.E. Haber et al., Nucl. Phys. B **161**, 493 (1979)
11. S. Kanemura, Eur. Phys. J. C **17**, 473 (2000)
12. A. Djouadi, J. Kalinowski, P.M. Zerwas, Z. Phys. C **57**, 569 (1993)
13. A.G. Akeroyd, Nucl. Phys. B **544**, 557 (1999)
14. A.G. Akeroyd, A. Arhrib, E. Naimi, Eur. Phys. J. C **20**, 51 (2001)
15. OPAL Collaboration, K. Ackerstaff et al., Phys. Lett. B **426**, 180 (1998)
16. OPAL Collaboration, G. Abbiendi et al., Eur. Phys. J. C **7**, 407 (1999)
17. ALEPH Collaboration, A. Heister et al., Phys. Lett. B **543**, 1 (2002)
18. DELPHI Collaboration, J. Abdallah et al., Eur. Phys. J. C **34**, 399 (2004)
19. L3 Collaboration, P. Achard et al., Phys. Lett. B **575**, 208 (2003)
20. OPAL Collaboration, K. Ahmet et al., Nucl. Instrum. Methods A **305**, 275 (1991)
21. B.E. Anderson et al., IEEE Trans. Nucl. Sci. **41**, 845 (1994)
22. S. Anderson et al., Nucl. Instrum. Methods A **403**, 326 (1998)
23. G. Aguillion et al., Nucl. Instrum. Methods A **417**, 266 (1998)
24. OPAL Collaboration, G. Abbiendi et al., Eur. Phys. J. C **26**, 479 (2003)
25. G. Ganis, P. Janot, in *Physics at LEP2*, CERN 96-01, vol. 2 (CERN, Geneva, 1996), p. 309
26. T. Sjöstrand, Comput. Phys. Commun. **82**, 74 (1994)
27. T. Sjöstrand, LU TP 95-20 (1995)
28. S. Jadach, B.F.L. Ward, Z. Wąs, Comput. Phys. Commun. **130**, 260 (2000)
29. S. Jadach, B.F. Ward, Z. Wąs, Phys. Lett. B **449**, 97 (1999)
30. J. Fujimoto et al., Comput. Phys. Commun. **100**, 128 (1997)
31. J. Fujimoto et al., in *Physics at LEP2*, CERN 96-01, vol. 2 (CERN, Geneva, 1996), p. 30
32. S. Jadach, W. Placzek, B.F.L. Ward, in *Physics at LEP2*, CERN 96-01, vol. 2 (CERN, Geneva, 1996), p. 286; UTHEP-95-1001

33. D. Karlen, Nucl. Phys. B **289**, 23 (1987)
34. S. Jadach, B.F.L. Ward, Z. Wąs, Comput. Phys. Commun. **79**, 503 (1994)
35. E. Budinov et al., in *Physics at LEP2, CERN 96-01*, vol. 2 (CERN, Geneva, 1996), p. 216
36. R. Engel, J. Ranft, Phys. Rev. D **54**, 4244 (1996)
37. G. Marchesini et al., Comput. Phys. Commun. **67**, 465 (1992)
38. J.A.M. Vermaseren, Nucl. Phys. B **229**, 347 (1983)
39. OPAL Collaboration, G. Alexander et al., Z. Phys. C **69**, 543 (1996)
40. F.A. Berends, R. Pittau, R. Kleiss, Comput. Phys. Commun. **85**, 437 (1995)
41. S. Jadach, W. Płaczek, M. Skrzypek, B.F.L. Ward, Z. Wąs, Comput. Phys. Commun. **119**, 272 (1999)
42. S. Jadach, W. Płaczek, M. Skrzypek, B.F.L. Ward, Z. Wąs, Comput. Phys. Commun. **140**, 475 (2001)
43. J. Allison et al., Nucl. Instrum. Methods A **317**, 47 (1992)
44. OPAL Collaboration, G. Abbiendi et al., Eur. Phys. J. C **32**, 453 (2004)
45. OPAL Collaboration, G. Abbiendi et al., Eur. Phys. J. C **18**, 425 (2001)
46. N. Brown, W.J. Stirling, Phys. Lett. B **252**, 657 (1990)
47. S. Bethke, Z. Kunszt, D. Soper, W.J. Stirling, Nucl. Phys. B **370**, 310 (1992)
48. S. Catani et al., Phys. Lett. B **269**, 432 (1991)
49. N. Brown, W.J. Stirling, Z. Phys. C **53**, 629 (1992)
50. OPAL Collaboration, G. Abbiendi et al., Eur. Phys. J. C **13**, 1 (2000)
51. OPAL Collaboration, G. Abbiendi et al., Eur. Phys. J. C **18**, 447 (2001)
52. M.H. Seymour, Nucl. Phys. B **436**, 163 (1995)
53. Mark J Collaboration, D.P. Barber et al., Phys. Rev. Lett. **43**, 830 (1979)
54. OPAL Collaboration, R. Akers et al., Z. Phys. C **67**, 365 (1995)
55. G. Hanson et al., Phys. Rev. Lett. **35**, 1609 (1975)
56. P. Bock, J. High Energy Phys. **01**, 080 (2007)
57. ALEPH, DELPHI, L3, OPAL and SLD Collaborations, LEP Electroweak Working Group, SLD Electroweak and Heavy Flavour Groups, S. Schael et al., Phys. Rep. **427**, 257 (2006)
58. Particle Data Group, C. Amsler et al., Phys. Lett. B **667**, 1 (2008)